JOURNAL OF GEOPHYSICAL RESEARCH: SOLID EARTH, VOL. 118, 1–20, doi:10.1002/2013JB010380, 2013

The seismic cycle at subduction thrusts: Insights from seismo-thermo-mechanical models

Y. van Dinther,[1,2] T. V. Gerya,[2] L. A. Dalguer,[1] P. M. Mai,[3] G. Morra,[4] and D. Giardini[2]

Received 29 May 2013; revised 6 November 2013; accepted 8 November 2013.

[1] The underestimation of the size of recent megathrust earthquakes illustrates our limited understanding of their spatiotemporal occurrence and governing physics. To unravel their relation to associated subduction dynamics and long-term deformation, we developed a 2-D continuum viscoelastoplastic model that uses an Eulerian-Lagrangian finite difference framework with similar on- and off-fault physics. We extend the validation of this numerical tool to a realistic subduction zone setting that resembles Southern Chile. The resulting quasi-periodic pattern of quasi-characteristic *M*8–*M*9 megathrust events compares quantitatively with observed recurrence and earthquake source parameters, albeit at very slow coseismic speeds. Without any data fitting, surface displacements agree with GPS data recorded before and during the 2010 *M*8.8 Maule earthquake, including the presence of a second-order flexural bulge. These surface displacements show cycle-to-cycle variations of slip deficits, which overall accommodate ~5% of permanent internal shortening. We find that thermally (and stress) driven creep governs a spontaneous conditionally stable downdip transition zone between temperatures of ~350°C and ~450°C. Ruptures initiate above it (and below the forearc Moho), propagate within it, interspersed by small intermittent events, and arrest below it as ductile shearing relaxes stresses. Ruptures typically propagate upward along lithological boundaries and widen as pressures drop. The main thrust is constrained to be weak due to fluid-induced weakening required to sustain regular subduction and to generate events with natural characteristics (fluid pressures of ~75–99% of solid pressures). The agreement with a range of seismological, geodetic, and geological observations demonstrates the validity and strength of this physically consistent seismo-thermo-mechanical approach.

Citation: van Dinther, Y., T. V. Gerya, L. A. Dalguer, P. M. Mai, G. Morra, and D. Giardini (2013), The seismic cycle at subduction thrusts: Insights from seismo-thermo-mechanical models, *J. Geophys. Res. Solid Earth*, *118*, doi:10.1002/2013JB010380.

1. Introduction

[2] Earthquakes occurring in convergent margins released approximately 90% of the last centuries seismic moment [e.g., *Pacheco and Sykes*, 1992]. They caused enormous human and economic loss as recently observed in Japan (2011 *M*9.0 Tohoku), Chile (2010 *M*8.8 Maule), and Indonesia (2004 *M*9.2 Sumatra). The physical mechanisms governing the spatiotemporal pattern of these megathrust earthquakes, however, elude us. This is illustrated in the Japanese region of Tohoku where an earthquake of *M*9.0 was deemed highly improbable for several reasons, including the combination of regional parameters governing subduction dynamics [*Stein et al.*, 2012; *Kagan and Jackson*, 2013]. To improve the understanding of why and where these earthquakes happen and when they might recur, physics-based numerical modeling tools are necessary. They have the potential to overcome the limited direct observables in both space and time. Therefore, we are developing a new physically consistent seismo-thermo-mechanical cycling approach (STM) in which active fault planes, geometries, and material properties evolve in response to amongst others tectonic stresses, temperatures, and pressures. This physics-based approach can lead to new insights into the cause-and-effect relations between subduction dynamics, long-term deformation features, and seismicity.

[3] Various numerical modeling approaches have been developed to investigate the seismic cycle [*Lapusta and Barbot*, 2012, and references therein] at subduction thrusts [*van Dinther et al.*, 2013, and references therein]. However, a comprehensive long-term numerical model of a realistic subduction zone that includes the three key ingredients—slow tectonic loading, rate-dependent friction, and viscoelastic stress relaxation of the mantle—does not exist yet [*Wang*, 2007]. Several approaches include both slow

Additional supporting information may be found in the online version of this article.

[1]Swiss Seismological Service, ETH Zürich, Zürich, Switzerland.
[2]Institute of Geophysics, ETH Zürich, Zürich, Switzerland.
[3]Division of Physical Sciences and Engineering, KAUST, Thuwal, Saudi Arabia.
[4]School of Geosciences, Department of Physics, University of Louisiana, Lafayette, Louisiana, USA.

Corresponding author: Y. van Dinther, Swiss Seismological Service, ETH Zürich, Sonneggstrasse 5, CH-8092 Zürich, Switzerland. (ylona.vandinther@erdw.ethz.ch)

2169-9313/13/10.1002/2013JB010380

tectonic loading and rate-dependent friction [e.g., *Kaneko et al.*, 2010], but these methods typically lack permanent deformation. In contrast, models that do include viscous stress relaxation predefine either slip or stress drop [e.g., *Hirahara*, 2002] or do not resolve slow tectonic loading [e.g., *Heimpel*, 2006].

[4] These approaches typically simulate subduction on an a priori defined, planar fault plane. Certain continuum approaches simulate self-consistent evolution of coseismic ruptures on evolving fault planes, like the damage rheology model for irreversible brittle deformation [e.g., *Lyakhovsky and Ben-Zion*, 2008]. These approaches typically focus on short time scales and ignore permanent deformation, although the long-term evolution has been studied for strike-slip fault systems [e.g., *Lyakhovsky and Ben-Zion*, 2009; *Finzi et al.*, 2009]. In a subduction setting the long-term geometric and material evolution feedback on the seismic cycle is ignored, but for a viscoelastoplastic laboratory model [*Rosenau et al.*, 2009; *Rosenau and Oncken*, 2009]. Numerical models, however, offer more flexibility and a more realistic geometry and rheology.

[5] The continuum viscoelastoplastic approach further developed in this paper [*Gerya and Yuen*, 2007; *van Dinther et al.*, 2013] has the potential to fill this gap and bridge seismological and geological observational time scales. The self-consistent evolution of coseismic rupture nucleation and propagation and subsequent long-term evolution of interface geometry and surface topography is driven by a kinematic ridge push and a dynamic slab pull (gravity and lower density mantle). This leads to spontaneous slab bending and interface locking guided by feedbacks due to the evolving temperature, stress, pressure, and compositional distributions. This unified physical framework guides both the fault zone and medium response. It has an approximated free surface, an incompressible inertia implementation, and it allows for large deformations.

[6] The seismic cycle applicability of this continuum viscoelastoplastic approach was demonstrated through validation against an innovative laboratory model [*Corbi et al.*, 2013; *van Dinther et al.*, 2013]. This validation demonstrated that comparable fast frictional instabilities are generated if friction varies similarly with slip rate. The resulting simple wedge model captured a range of physical phenomena observed in nature, including (a) ruptures that (back-) propagate as cracks or self-healing pulses and (b) afterslip that complements surface displacements during the postseismic period. The current study extends the laboratory validation to a more realistic setup of the Southern Chilean convergent margin through a comparison to a variety of natural observations. The validation is extended by highlighting several interesting implications that result from physically consistent feedback mechanisms.

[7] A description of the seismo-thermo-mechanical numerical modeling approach (section 2) is followed by an analysis of the model's physical characteristics and spatiotemporal megathrust pattern (section 3.1). In section 3.2 we analyze the corresponding interseismic, coseismic, and postseismic surface displacements, which are shown to agree surprisingly well with interseismic and coseismic GPS measurements in Southern Chile. Subsequently, the analysis of underlying stresses and strengths at the thrust reveals that temperature mainly governs downdip rupture characteristics in this specific setup (section 3.3). Finally, a parameter study on fault strength shows that both fluid-induced and frictional weakening are necessary and noninterchangeable (section 3.4). These findings and their limitations and implications are then discussed in broader perspective, highlighting the correspondence to a wide range of natural observations (section 4). Two appendices provide details on the selection of frictional parameters (Appendix A) and on the sensitivity of the model results to subduction velocity and mantle shear modulus and viscosity (Appendix B).

2. Method

[8] We adopt the viscoelastoplastic, continuum mechanics thermomechanical code I2ELVIS [*Gerya and Yuen*, 2007]. This code has been validated for seismic cycle applications using an iso-viscoelastic, purely mechanical version [*van Dinther et al.*, 2013], while the long-term evolution of temperature is benchmarked separately [*Gerya and Yuen*, 2003a]. Below we briefly summarize the method provided in more detail in *van Dinther et al.* [2013], while focusing on the additional components relevant for simulating seismogenesis in a realistic subduction zone. This includes solving the heat equation; using stress-, pressure-, and temperature-dependent viscous flow laws; and the treatment of (de)hydration, fluid flow, and erosional processes. These processes act upon a self-consistent model that simulates the subduction of an oceanic slab below a continent, which is driven both by an applied kinematic ridge push and spontaneous slab pull.

2.1. Governing Equations

[9] The two-dimensional thermomechanical code uses an implicit, conservative finite difference scheme on a fully staggered Eulerian grid in combination with a Lagrangian marker-in-cell technique. The code solves for the conservation of mass, momentum, and energy. The Lagrangian markers track lithology, corresponding properties and stress histories, as they are advected according to the velocity field and leave the Eulerian grid undeformed [e.g., *Brackbill and Ruppel*, 1986; *Gerya and Yuen*, 2003b].

[10] The following three mechanical equations are solved to obtain the horizontal and vertical velocities, v_x and v_z, and pressure P (defined as the mean stress)

$$\frac{\partial v_x}{\partial x} + \frac{\partial v_z}{\partial z} = 0, \tag{1}$$

$$\frac{\partial \sigma'_{xx}}{\partial x} + \frac{\partial \sigma'_{xz}}{\partial z} - \frac{\partial P}{\partial x} = \rho \frac{Dv_x}{Dt}, \tag{2}$$

$$\frac{\partial \sigma'_{zx}}{\partial x} + \frac{\partial \sigma'_{zz}}{\partial z} - \frac{\partial P}{\partial z} = \rho \frac{Dv_z}{Dt} - \rho g. \tag{3}$$

[11] The continuity equation (1) assumes an incompressible medium. The equations of motion (2) and (3) are written in terms of deviatoric stress tensor components σ'_{ij} and include gravity acceleration g (= 9.81 m/s^2) and incompressible inertia (i.e., including shear waves but not pressure waves). The inertial term is represented by density ρ times the Lagrangian time derivative of the respective velocity components $\frac{Dv}{Dt}$ and stabilizes high slip rates at small time steps [*van Dinther et al.*, 2013].

[12] In the same framework, solving the Lagrangian form of the energy equation provides temperature T and is given by

$$\rho C_p \left(\frac{DT}{Dt}\right) = -\frac{\partial q_x}{\partial x} - \frac{\partial q_z}{\partial z} + H_a + H_s + H_r, \tag{4}$$

$$q_x = -k\frac{\partial T}{\partial x}, q_z = -k\frac{\partial T}{\partial z}, \tag{5}$$

$$H_a = T\alpha_\rho \left(v_x\frac{\partial P}{\partial x} + v_z\frac{\partial P}{\partial z}\right), \tag{6}$$

$$H_s = \sigma'_{xx}(\dot{\varepsilon}'_{xx} - \dot{\varepsilon}'_{xx,\mathrm{elastic}}) + \sigma'_{zz}(\dot{\varepsilon}'_{zz} - \dot{\varepsilon}'_{zz,\mathrm{elastic}}) + 2\sigma'_{xz}(\dot{\varepsilon}'_{xz} - \dot{\varepsilon}'_{xz,\mathrm{elastic}}). \tag{7}$$

[13] Here thermal conductivity k and density depend on temperature and rock composition c. C_p is isobaric heat capacity, DT/Dt is the Lagrangian time derivative of temperature, and q_x and q_z are the horizontal and vertical heat flux, respectively. α_ρ is the thermal expansion coefficient and $\dot{\varepsilon}'_{ij}$ refers to the deviatoric strain rate tensor components. This energy equation includes contributions from conductive heat transport and volumetric internal heat generation H due to adiabatic (de)compression H_a, shear heating during nonelastic deformation H_s, and lithology-specific radioactive heat production H_r [e.g., *Gerya and Yuen*, 2007].

2.2. Rheological Model

[14] These equations are solved using constitutive relations that relate deviatoric stresses and strain rates in a nonlinear viscoelastoplastic manner according to

$$\dot{\varepsilon}'_{ij} = \frac{1}{2\eta}\sigma'_{ij} + \frac{1}{2G}\frac{D\sigma'_{ij}}{Dt} + \begin{cases} 0 & \text{for } \sigma'_{\mathrm{II}} < \sigma_{\mathrm{yield}} \\ \chi\frac{\partial g_{\mathrm{pl}}}{\partial \sigma'_{ij}} & \text{for } \sigma'_{\mathrm{II}} = \sigma_{\mathrm{yield}} \end{cases} \tag{8}$$

[15] In these relations η is effective viscosity and G is shear modulus. $D\sigma'_{ij}/Dt$ is the objective corotational time derivative solved using a time explicit scheme [e.g., *Moresi et al.*, 2003]. χ is a plastic multiplier connecting plastic strain rates and stresses and g_{pl} is the plastic flow potential. σ'_{II} is the second invariant of the deviatoric stress tensor ($\sqrt{\sigma'^2_{xx} + \sigma'^2_{xz}}$), which is compared to the local plastic strength σ_{yield}. The amount of elastic versus viscous deformation is determined by the viscoelasticity factor $(G\Delta t)/(G\Delta t + \eta_{\mathrm{vp}})$ [e.g., *Moresi et al.*, 2003; *Gerya*, 2010a]. The end-member elastic and viscous rheological behaviors are fully regained if the computational time step Δt times shear modulus is respectively much smaller or much larger than the effective viscoplastic viscosity η_{vp}. This viscosity-like Lagrangian parameter is η if plastic deformation is absent and $\eta\frac{\sigma'_{\mathrm{II}}}{\eta\chi+\sigma'_{\mathrm{II}}}$ if plastic yielding occurs.

[16] The nonlinear creep viscosity η is defined as a function of temperature, pressure, and stress and follows experimentally determined dislocation creep flow laws. It can be written as a function of the second deviatoric stress invariant [e.g., *Ranalli*, 1995] as

$$\eta = \left(\frac{1}{\sigma'_{\mathrm{II}}}\right)^{(n-1)} \cdot \frac{1}{2A_D} \cdot \exp\left(\frac{E_a + PV_a}{RT}\right), \tag{9}$$

where R is the gas constant (8.314 J/(mol·°C). Stress exponent n, preexponential factor A_D, activation energy E_a, and activation volume V_a are experimentally determined rheological parameters set for each lithology.

2.3. Hydration and Fluid Flow Processes

[17] We simulate temperature, pressure, and depth-driven slab dehydration and resulting long-term fluid flow processes in a thermodynamically and petrologically consistent manner [e.g., *Gerya and Meilick*, 2011]. Long-term fluid flow means that we neglect short-term spatiotemporal variations of pore fluid pressures, i.e., hydraulic properties and pore fluid pressures are constant [e.g., *Faccenda et al.*, 2009]. We rather self-consistently solve on what locations fluids will be present. At these locations material strength is reduced (section 2.4), thereby playing an important role in the generation of earthquakes [e.g., *Saffer and Tobin*, 2011].

[18] At the onset of subduction, water is contained within the crystal structures of ocean floor sediments and the oceanic crust [*Gerya and Meilick*, 2011]. Additionally, 1 wt% of pore water is present within the pores of the altered top of the oceanic crust and sediments. As the slab subducts, water is released both due to metamorphic dehydration reactions and compaction. As pressure and temperature increase, metamorphic reactions release water as crystal structures are able to contain less water [e.g., *Peacock*, 1993; *Gerya and Meilick*, 2011]. The in situ water content of a rock assemblage is computed based on thermodynamic equilibrium following a Gibbs free energy minimization approach [*Connolly*, 2005; *Gerya et al.*, 2006]. The compaction of basalt and sediments leads to the release of pore fluids as porosity decreases with depth. This is described by a function in which the pore water content decreases linearly from 1 wt% at 0 km to 0 wt% at 75 km. Based on the newly calculated maximum water content (both mineralogical and porous) of a small volume (represented by a rock marker), excess water is released (i.e., a fluid marker is formed). The free water migrates through the deforming rocks until it is (partially) consumed by a rock assemblage able to do so. Migrating fluids follow the path of the highest pressure gradient [e.g., *Faccenda et al.*, 2009] at speeds $v_{x,\mathrm{water}}$ and $v_{z,\mathrm{water}}$ of

$$v_{x,\mathrm{water}} = v_x - \frac{v_{\mathrm{per}}}{(\rho_m - \rho_f)g}\left(\frac{\partial P}{\partial x}\right), \tag{10}$$

$$v_{z,\mathrm{water}} = v_z - \frac{v_{\mathrm{per}}}{(\rho_m - \rho_f)g}\left(\frac{\partial P}{\partial z} - \rho_f g\right). \tag{11}$$

[19] In these equations, v_x and v_z represent the local rock velocities and ρ_m and ρ_f are the mantle (3300 kg/m^3) and fluid (1000 kg/m^3) densities, respectively. v_{per} indicates the relative upward velocity of the percolating fluid (0.1 cm/yr) [*Gorczyk et al.*, 2007]. This relatively low velocity of relative water percolation is adopted to reduce the extent of serpentinization of the upper plate and simplify the lithological structure of the plate interface.

2.4. Plasticity and Friction Formulations

[20] The brittle faulting process is represented by nonassociated Drucker-Pager plasticity [*Drucker and Prager*, 1952], as routinely done in geodynamics [e.g., *Poliakov et al.*, 1993; *Buiter et al.*, 2006]. This yielding model limits the second invariant of the deviatoric stress tensor at each marker by the pressure-dependent yield stress σ_{yield}

$$\sigma_{\mathrm{yield}} = C + \mu \cdot \left(1 - \frac{P_f}{P_s}\right) \cdot P, \tag{12}$$

where C is cohesion and μ is the effective friction coefficient, calculated as a function of slip rate and temperature-dependent properties. P_f/P_s represents the pore fluid pressure factor λ. To satisfy the yielding criterion and to maintain local equilibrium between deviatoric stresses and strain rates, the local viscosity is decreased. This weakens the material and localizes deformation around that marker. This Lagrangian approach provides a local invariant formulation that does not require the a priori definition of a fault plane. The evolving rupture rather selects a path as a function of the local stress and strength field.

[21] The pore fluid pressure factor λ represents the reduction of frictional sliding resistance due to the pore fluids, whose pressure P_f opposes the acting solid rock pressures P_s (=P). For dry rocks, a pore fluid pressure factor of 0 is assumed, except for the shallowest 5000 m over which λ linearly decreases from a hydrostatic gradient of 0.4 at the surface to 0. This highly simplified implementation mimics the increase of brittle rock strength with depth due to the absence of fluids in dry rocks. However, if migrating pore fluids are present, rocks in a radius of 2000 m are assumed to be subjected to increased pore fluid pressures.

[22] A friction coefficient dependent on slip velocity is crucial to simulate brittle instabilities or analog earthquakes with this continuum approach [*van Dinther et al.*, 2013]. Sufficient coseismic weakening and subsequent healing is obtained through a strongly rate-dependent friction formulation [e.g., *Burridge and Knopoff*, 1967; *Cochard and Madariaga*, 1994; *Ampuero and Ben Zion*, 2008]. We calculate the effective steady state friction coefficient at every marker as a function of slip rate V as

$$\mu = \mu_s(1-\gamma) + \mu_s \frac{\gamma}{1+\frac{V}{V_c}}. \tag{13}$$

[23] In equation (13) μ_s is the static friction coefficient and γ is the maximum amount of weakening that can be induced by increasing slip rate. γ is equivalent to $-(\alpha-\beta)/\mu_s$, where α and β quantify the direct and evolution effect, respectively. These are related to a and b in classical rate-and-state friction formulations [*Ampuero and Ben Zion*, 2008]. The minimum dynamic friction coefficient μ_d is $\mu_s \cdot (1-\gamma)$, which is asymptotically approached as $1/V$. If $\gamma > 0$ (or $\alpha - \beta$ is negative), this formulation results in velocity-weakening behavior, so that a decrease of strength initiates an instability and introduces stick-slip dynamics. If $\gamma < 0$, velocity-strengthening behavior or stable slip results as a strength increase inhibits instabilities. Finally, V_c is the characteristic slip velocity at which half of the friction drop will have occurred. This characteristic value normalizes the local viscoplastic slip velocity V, which is calculated as the velocity difference between two nodal interfaces and represented by the viscoplastic strain rate $\sigma_{\text{yield}}/\eta_m$ times the grid size dx. Here η_m denotes the local viscosity from the previous time step. This grid size-dependent scheme cancels the change of strain rate with grid size and introduces a length scale into the inherent grid size-dependent plasticity problem [e.g., *Needleman*, 1988; *Lavier et al.*, 2000; *van Dinther et al.*, 2013].

2.5. Model Setup

[24] We model a 1500 × 200 km^2 trench-normal section of the Southern Chilean convergent margin in which the oceanic Nazca slab subducts into the upper mantle beneath the continental South American plate (Figure 1a). Subduction is forced by imposing a constant plate velocity nearly 500 km seaward of the trench (Figure 1a). The initiation of subduction is facilitated by an initial weak zone that follows a wet olivine flow law and has a very low plastic strength [e.g., *Gerya and Meilick*, 2011]. As subduction progresses, the oceanic crust replaces this weak material and the system assumes a stable slab dip and geometry. This configuration is consistent with, e.g., imposed velocities, interface strength, and surrounding mantle and lithosphere properties (Figure 1b). After 5.1 My, a starting configuration (t = 0) with a stable geometry and stress state was obtained by stepwise reducing time steps and increasing interface strength.

[25] The configuration resembles the continental margin in Southern Chile around 36°S (Figure 1, as used in e.g., *Gorczyk et al.* [2007]). This margin recently experienced two megathrust earthquakes: the 1960 *M*9.5 Valdivia and 2010 *M*8.8 Maule events. Seismic refraction profiles and gravity and local tomography data provide the suggested lithological boundaries and indicate a ~25 km deep and 150 km wide (paleo-)sedimentary wedge [e.g., *Krawczyk et al.*, 2006]. The subduction velocity of 7.5 cm/yr and thermal slab-cooling age of 40 My are constrained for Southern Chile from a geodynamic database [*Heuret and Lallemand*, 2005].

2.6. Material Parameters

[26] The model comprises upper and lithospheric mantle (anhydrous peridotite), continental and oceanic crust, and a prism of sediments (Figure 1). The oceanic crust is composed of 5 km thick gabbro overlain by 2 km of fractured and hydrated oceanic upper crust, which is modeled using a wet quartzite rheology. This simulates the simultaneous presence of subducted sediments and potential overriding crust slices within the rock melange that forms the Southern Chile 3–7 km wide subduction channel [e.g., *Shreve and Cloos*, 1986; *Lohrmann et al.*, 2006; *Fagereng and Sibson*, 2010]. The (numerical) subduction channel contains several fault zones of spontaneously forming, continuously switching active thrust interfaces. Additionally, dehydration at low velocities adds a thin ~1 km layer of serpentinites below the overriding plate's lithospheric mantle (Figure 1b). The thermomechanical parameters and flow laws corresponding to these lithologies comply with previously used data sets [e.g., *Gerya et al.*, 2006; *Gorczyk et al.*, 2007; *Faccenda et al.*, 2008; *Gerya*, 2010b; *Gerya and Meilick*, 2011] (Table 1).

[27] The plastic/brittle parameters used correspond to recent slip rate-dependent laboratory data (Table 1). The frictional properties of the subduction thrust interface are guided by temperature-dependent laboratory experiments on wet illite-rich gouge [*den Hartog et al.*, 2012] (Appendix A, Figure 2). These laboratory data indicate a velocity-weakening domain surrounded by an updip and downdip domain with velocity strengthening (model 3 in Figure 2). In the reference model, however, we exclude the downdip velocity-strengthening domain to analyze the self-consistent effects of temperature, stress, and geometry (red thick line for model 2 in Figure 2). In model 1 we exclude both velocity-strengthening domains.

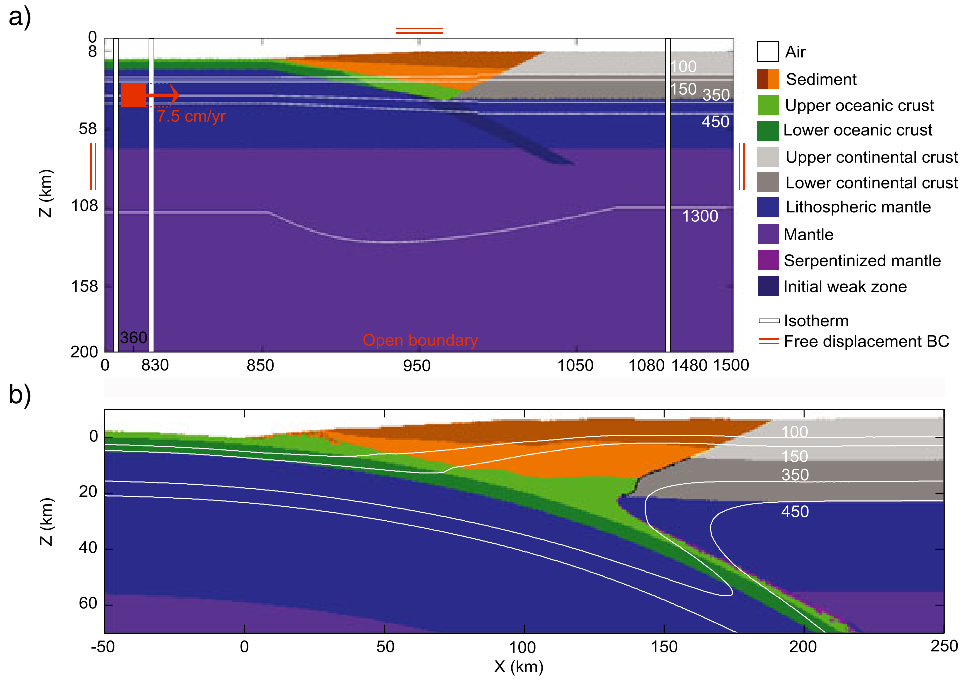

Figure 1. Model configuration depicting lithology (in color) overlain by isotherms (in white and °C). (a) Initial configuration for the entire model domain, including mechanical boundary conditions in red. (b) Zoom of starting configuration after 5.1 My of subduction ($t=0$). The axis values are from here onward, shown with respect to the bathymetric minimum, i.e., the trench.

[28] Cohesion or residual strength assumed for the thrust interface is relatively low (6 MPa) [*Schultz*, 1995]. This assumption reflects the significant degree of fracturing and damage that occurred during ongoing subduction. Cohesion for all other rock types is set to 200 MPa to inhibit plasticity outside the thrust interface, once we decrease time steps to go toward the initial configuration. This simplification allows us to focus our analysis on interplate seismicity, as in the laboratory validation study [*van Dinther et al.*, 2013].

[29] The pore fluid pressure factor λ (P_f/P_s) is set to 0.95 based on differential stress predictions for the Southern Chilean margin [*Seno*, 2009]. This factor is varied over a wide range in a parametric study to evaluate its impact on interplate seismicity, stress levels, and thrust interface orientation.

2.7. Initial and Boundary Conditions

[30] A free displacement (or free slip) mechanical boundary condition acts at the top and side boundaries. The lower boundary is vertically penetrable and assumes that external free slip is satisfied at a depth of 500 km [*Gorczyk et al.*, 2007] (Figure 1a). The top boundary is treated as an approximated internal free surface by using 8–12.5 km of air with a very low viscosity ($1\cdot10^{17}$ Pa·s) and density (1 kg/m^3) to minimize shear stresses [e.g., *Schmeling et al.*, 2008]. The shear modulus of the air is set to 700 GPa to ensure the air behaves as a fully viscous body at each time step

Table 1. Rheological Parameters of Relevant Materials[a]

Material	Flow Law	η_0	n	E_a	V_a	G	ρ_0^{d}	k^{e}	H_r	μ_s	C
Sediments	Wet quartzite[b]	$1.97\cdot10^{17}$	2.3	$1.54\cdot10^5$	0.80	10	2600	$[0.64+807/(T+77)]\cdot\exp(4\ 10^{-5}P)$	2	0.35[f]	200
Upper cont. crust	Wet quartzite	$1.97\cdot10^{17}$	2.3	$1.54\cdot10^5$	1.20	25	2700	$[0.64+807/(T+77)]\cdot\exp(4\ 10^{-5}P)$	1	0.72[g]	200
Lower cont. crust	Wet quartzite	$1.97\cdot10^{17}$	2.3	$1.54\cdot10^5$	1.20	25	2700	$[0.64+807/(T+77)]\cdot\exp(4\ 10^{-5}P)$	1	0.72[g]	200
Upper oceanic crust	Wet quartzite	$1.97\cdot10^{17}$	2.3	$1.54\cdot10^5$	0.80	25	3000	$[1.18+474/(T+77)]\cdot\exp(4\ 10^{-5}P)$	0.25	0.50[h]	6[l]
Lower oceanic crust	Plagioclase[b]	$4.80\cdot10^{22}$	3.2	$2.38\cdot10^5$	0.80	25	3000	$[1.18+474/(T+77)]\cdot\exp(4\ 10^{-5}P)$	0.25	0.85[i]	200
Lithosphere mantle	Dry olivine[b]	$3.98\cdot10^{16}$	3.5	$5.32\cdot10^5$	0.80	67	3300	$[0.73+1293/(T+77)]\cdot\exp(4\ 10^{-5}P)$	0.022	0.60[j]	200
Mantle	Dry olivine	$3.98\cdot10^{16}$	3.5	$5.32\cdot10^5$	0.80	67	3300	$[0.73+1293/(T+77)]\cdot\exp(4\ 10^{-5}P)$	0.022	0.60[j]	200
Serpentinized mantle	Antigorite[c]	$3.21\cdot10^{36}$	3.8	$8.90\cdot10^3$	0.32	67	3000	$[0.73+1293/(T+77)]\cdot\exp(4\ 10^{-5}P)$	0.022	0.52[k]	200

[a]Other properties for all rock types are $\alpha_\rho=3\cdot10^{-5}$ K^{-1} and β_ρ=$1\cdot10^{-5}$ MAP^{-1} that make $\rho=\rho_0\cdot[1-\alpha_\rho(T-298)]\cdot[1+\beta_\rho(P-0.1)]$ and $C_p=1000$ J/kg/K and γ=0.7. η_0 is the reference viscosity in Pa^n s and is equal to the preexponential exponent 1/Ad in equation (9). E_a is in J, V_a is in J/bar, G is in GPa, ρ_0 is reference density in kg/m^3, k is in W/m/K (at T_K, P_{MPa}), H_r is in μW/m^3, and C is in MPa. [b]*Ranalli* [1995]; [c]*Hilairet et al.* [2007]; [d]*Turcotte and Schubert* [2002]; *Bittner and Schmeling* [1995]; [e]*Clauser and Huenges* [1995]; *Hofmeister* [1999]; [f]*den Hartog et al.* [2012]; [g]*Chester and Higgs* [1992]; [h]*Di Toro et al.* [2011]; [i]*Tsutsumi and Shimamoto* [1997]; [j]*Del Gaudio et al.* [2009]; [k]*Escartin et al.* [1997]; [l]*Schultz* [1995].

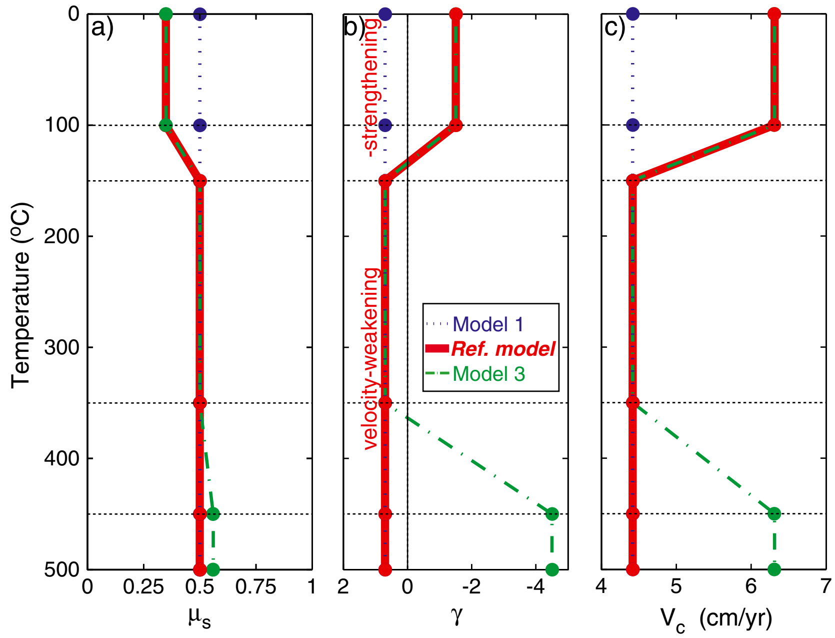

Figure 2. Friction parameters (equation (13)) with temperature for three different model setups: (1) purely velocity weakening, (2) including updip velocity strengthening (**reference model**), and (3) including downdip velocity strengthening. (a) Static friction coefficient μ_s, (b) amount of weakening γ $(1 - \frac{\mu_d}{\mu_s})$, and (c) characteristic velocity V_c. Values are guided by relations observed in *den Hartog et al.* [2012] (see Appendix A).

(i.e., $\Delta t/t_{\mathrm{Maxwell}} > 1000$). This sticky air approach ensures that topography is created consistently. Topographic evolution is affected by erosion, implemented through a transport equation at the Eulerian surface

$$\frac{\partial z_{\mathrm{es}}}{\partial t} = v_z - v_x \frac{\partial z_{\mathrm{es}}}{\partial x} + v_e, \tag{14}$$

where z_{es} is the vertical position of that surface and v_e is the gross-scale erosion rate of 0.03 cm/yr for $z_{\mathrm{es}} < 8$ km and 0 for $z_{\mathrm{es}} > 8$ km [*Gerya and Meilick*, 2011]. Low viscosity regions are prescribed next to the side walls and bottom boundary to allow for lithosphere decoupling and slab penetration, respectively. Additionally, lower and upper viscosity limits of $1{\cdot}10^{17}$ and $1{\cdot}10^{25}$ Pa·s are applied throughout the model.

[31] The initial temperature field (white contours in Figure 1a and subsequent figures) were calculated according to (a) an oceanic lithosphere of 40 Ma [*Turcotte and Schubert*, 2002], (b) a linearly increasing temperature from 0 to 1300°C for continental depths from 0 to 100 km, and (c) a temperature gradient of 0.5°C/km within the asthenospheric mantle. This initial profile evolves into a self-consistent thermal structure in response to time-dependent temperature changes due to subduction (equation (4)), while complying with thermal boundary conditions. These are set to 0°C at the top, zero heat flux at the sides, and an infinite-like constant temperature condition at the lower external boundary [*Gorczyk et al.*, 2007].

[32] To solve the above-described problem we utilize a 2-D nonuniform, fully staggered finite difference grid of 1466×270 nodes. This provides a grid size of 500 m within the 450×100 km zone of interest (and maximum 2000 m outside of it). Rock-specific properties and changes in physical quantities are tracked using 22.4 million markers. Time is traversed with computational and displacement time steps of 5 years, thereby smoothing most coseismic effects.

3. Results and Analysis

[33] This section analyzes the response of the reference model that has velocity-strengthening friction below temperatures of ~ 130°C and velocity-weakening friction for higher temperatures (model 2 in Figure 2). The simulated seismic cycles are characterized by partially locked interseismic periods, rapid coseismic seaward motions of the forearc, and relaxing postseismic responses [e.g., *Wang*, 2007; *van Dinther et al.*, 2013]. Throughout the manuscript, we refer to the region with thrust fault zone temperatures below about 150°C as "updip," while "downdip" refers to thrust temperatures above about 350°C and "active seismogenic zone" denotes the region in between. It is important to realize that this terminology is not a priori related to a predefined frictional stability, unless specifically mentioned.

3.1. Seismicity

[34] The physical state of the continental margin at the end of an interseismic period is depicted in Figure 3 (left column). The viscous strength profile in Figure 3a shows a strong oceanic slab subducting beneath a continent in which a weak lower crust is sandwiched between a stronger upper crust and continental lithospheric mantle. Effective viscosities along the subduction channel are low within horizontal distances of 75 km from the trench X or temperatures T below ~ 140°C, where the thrust is defined to creep aseismically. As temperatures (and stresses) increase, viscosities

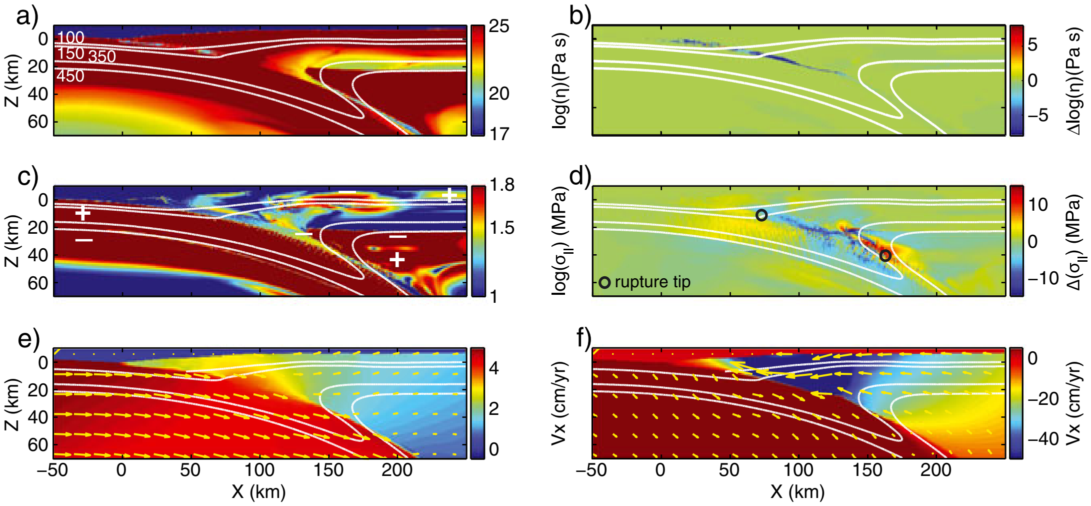

Figure 3. Main physical variables of the reference model (friction model 2 in Figure 2) (a, c, e) one time step before and (b, d, f) at the peak of the reference event. Variables are (a) effective viscosity η_{vp}, (b) viscosity difference with respect to Figure 3a, (c) second invariant of the deviatoric stress tensor, (d) stress difference with respect to Figure 3c, (e, f) horizontal velocity in color overlain by arrows indicating velocities (note that arrows in Figure 3f are 10 times smaller). All plots are overlain by white isotherms at 100°C, 150°C, 350°C, and 450°C. *X* refers to the landward distance from the trench, *Z* refers to the depth below the trench. Regions marked with crosses experience horizontal extension and those marked with hyphens experience horizontal compression.

start to decrease beyond 100 km, reaching near upper mantle values of $\sim 3 \cdot 10^{19}$ Pa·s at 180 km. These two low-viscosity regimes at the thrust lead to two lower stress regimes surrounding a high-viscosity, interseismically locked zone. Within this active seismogenic zone the second invariant of the deviatoric stresses increase with depth up to ~35 MPa (Figure 3c). The locking in this region is confirmed by a low slip zone between ~75 and ~130 km (Figure 3e). Beyond this zone, interseismic velocities within the overriding plate decrease. These velocities, however, increase again below the "interplate decoupling depth" [*Furukawa*, 1993] at 75 km, as mantle wedge material is dragged down along with the slab again.

[35] During the subsequent representative event, yielding of one specific upward-widening interface occurs as indicated by a drop in viscosity (Figure 3b). The selected rupture path varies from event to event in location and thickness depending on the local stress and strength field within the subduction channel. Most ruptures, however, propagate along the bottom of the composite subduction channel. Within this composite fault zone, we observe a stress drop along the rupture with respect to the start of the event (Figure 3d). Stress increases at the rupture tips and outside of the fault zone. Within the bending slab this increasing second invariant pattern is overprinted in two quadrants by compression in the outer extensional bend, downdip of the rupture, and extension in the inner compressional bend, updip of the rupture. As the slab decouples from the overriding plate, it subducts about five times faster in a more downward direction (Figure 3f). A more detailed analysis of this reference event is provided throughout these results. For a better visual understanding we refer to a movie in the supporting information.

[36] The reference event is typical for a series of 36 events recorded over 35,000 simulation years in which over 2000 m of slab displacement occurred. We use the method of *Corbi et al.* [2013] and *van Dinther et al.* [2013] to automatically identify seismic events and determine their source parameters. This uses a velocity threshold applied to the spatiotemporal evolution of thrust-parallel velocities at a line 6.4 km (1 cm in the laboratory) above the evolving thrust interface (Figure 4). White and gray colors depict landward motions of the forearc and illustrate the interseismic locking pattern. If seaward velocities (yellow to black) are faster than -15.6 cm/yr (3.8 times the interseismic velocity of the slowest slipping part as in *Corbi et al.* [2013]), a rupture is occurring. The word "rupture" here refers to the occurrence of rapid threshold-exceeding slip during which permanent displacement and stress drop occur along a localized interface. Its source parameters are defined based on the extremes of the velocity threshold (Figures 4b and 4c). The reference event nucleates near 125 km and ruptures as a bilateral crack that predominantly accelerates upward (Figure 4b).

[37] This method for detecting simulated seismic events reveals a regular series of large thrust events that have an average overriding plate displacement of 18 m (covering a range from 0.1 to 30 m) on average every 881 (236–1452) years (Figure 4a). These events have an average horizontal width of 114 (0.9–189) km. Using empirical scaling relations of *Blaser et al.* [2010], this width roughly scales to moment magnitudes of about 8.3 (3.9–9.0). These predominantly megathrust events are several orders of magnitude too slow with average rupture speeds of $2.8 \cdot 10^{-5}$ m/s and maximum displacement velocities of $2.6 \cdot 10^{-8}$ m/s. Ruptures thus last for an average of $5.1 \cdot 10^{7}$ min (97 years). The hypocenters (open circles) are typically located 120–140 km from the trench, where plate locking decreases spontaneously and interseismic slip thus increases (Figures 3e and 4a). Most ruptures then accelerate up to their peak velocity

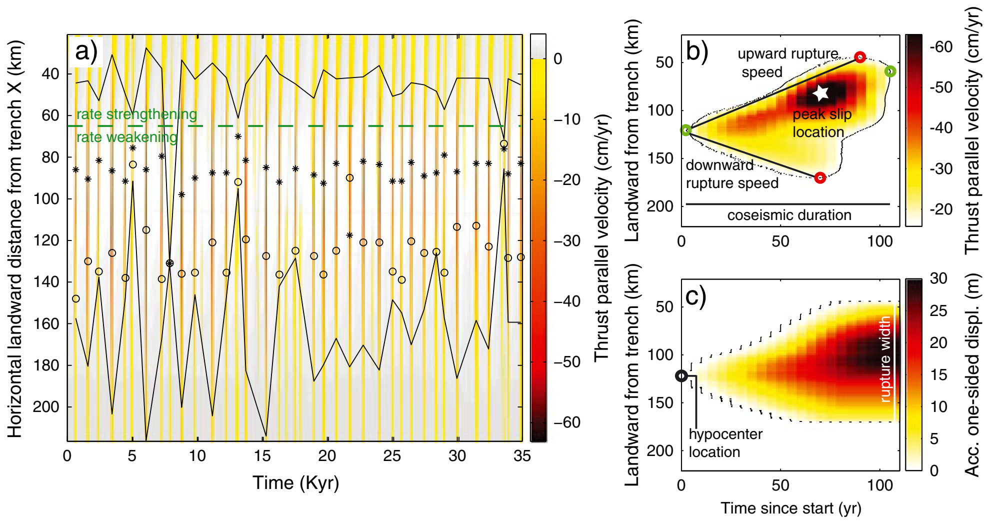

Figure 4. Spatiotemporal evolution of thrust-parallel velocity at 6.4 km above the thrust interface (determined by the vertically highest strain rate within the subduction channel) for (a) the simulation and (b) the reference event at $t = 26,390$ yr. In Figure 4a we add hypocenter location (open circle), peak slip location (star), and maximum rupture extent (lines) in black and imposed frictional stability limits in green. They are estimated from the red and green extremes of the black-dotted thrust-parallel velocity contour depicted in Figures 4b and 4c. Figure 4c shows the corresponding accumulated overriding plate displacement. Once averaged over space, this provides accumulated one-sided displacement (indicative of slip). Note that the true hypocenters are typically located 10 km more landward, as this distance is needed for the ruptures to accelerate and pass beyond the velocity threshold at 6.4 km above the thrust.

locations (stars) between 75 and 92 km, just below the defined velocity-strengthening updip limit.

[38] The regularity of these events is quantified using the coefficient of variation *Cv* [*Kuehn et al.*, 2008], which is calculated as the standard deviation over the average of a given distribution. The resulting values indicate that our event recurrence is quasi-periodic ($Cv_{rec.interval} = 0.3$, i.e., < 1) and quasi-characteristic ($Cv_{event.size} \approx 0.4$).

3.2. Surface Displacements

[39] Figure 5 provides an overview of the surface displacements recorded for the reference model with velocity-weakening friction below ~130°C (model 2 in Figure 2). Figures 5a and 5b depict a zoom of the temporal evolution of the respective horizontal and vertical components of an array of seven-colored markers that are ordered according to their distance to the trench (Figure 5f). Their displacement shows a horizontal sawtooth pattern of rapidly seaward moving events alternating with periods of slow landward displacement, as observed above the thrust in Figure 4. The complementary vertical displacement pattern is slightly more complex, but the main features correspond to an interseismically locked seismogenic zone that drags down the surface above it and hence creates interseismic uplift landward. The elastic strain accumulated during the interseismic periods is released by coseismic displacements in accordance with the elastic rebound concept [*Reid*, 1910]. Both horizontal and vertical displacements reveal a spatially varying postseismic delay before displacements reverse to their interseismic directions again.

[40] This time series of surface displacements reveals two other observations relating to the amount of coseismic displacement recovered, with respect to what was accumulated during the interseismic period (Figures 5a and 5b). First, this slip deficit varies from cycle to cycle and is not directly determined by the preceding amount of interseismic strain. The seismicity pattern is not distinctly time predictable. This is confirmed by a low regression coefficient R^2 between the duration of the preceding interseismic period and consequent mean slip ($R^2 = 0.23$) and consequent mean rupture width ($R^2 = 0.14$). An example of an event that recovers about one third more displacement than was accumulated is the reference event that experiences overshoot and thus has a negative slip deficit. Second, over the entire simulation about 5% of the interseismic displacement is not recovered during the coseismic period. This instead contributes to permanent anelastic deformation of the overriding plate.

[41] The spatial evolution of the reference event is illustrated in more detail in Figure 5 (right column). For a direct comparison with natural observations, we add GPS measurements from 28 stations recording during the interseismic period in 1996, 1999, and 2002 in Southern Chile [*Ruegg et al.*, 2009] and from 31 stations recording during the 2010 *M*8.8 Maule earthquake [*Vigny et al.*, 2011].

[42] The simulated spatial interseismic pattern shows two distinct hinge points at 115 and 255 km landward of the trench (Figure 5c). These locations correspond to the thrust intersection with the continental Moho and to the thrust intersection with the thermally defined continental lithosphere-asthenosphere boundary (T = 1300°C). The interseismic extremes show subsidence of ~5 m at 70 km and a maximum of 1.9 m uplift a few kilometers seaward of the spontaneous downdip limit of the seismogenic zone. This spatial pattern with regions of seismogenic subsidence, uplift, and again minor subsidence; the locations of the hinge points; and the corresponding magnitudes are approximately

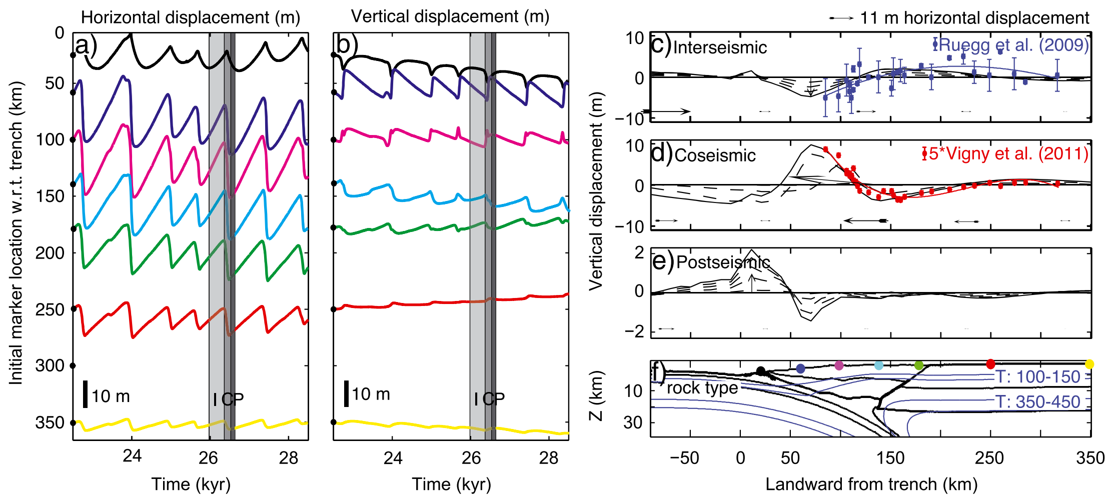

Figure 5. Surface displacements both depicted in time, (a) in horizontal (+ = landward) and (b) vertical (+ = upward) directions, and in space, as accumulated vertically (dashed lines are intermediates; solid line is total) and horizontally (arrows show total) during the (c) interseismic (I), (d) coseismic (C), and (e) 110 yr postseismic (P) period of the reference event (model 2). In Figures 5a and 5b displacements are ordered according to distance to the trench but show displacements in meters according to the inset. Figures 5c and 5d are overlain by GPS data points obtained in Southern Chile between 35°S and 37.5°S with respect to a stable South America for the interseismic period (blue: *Ruegg et al.* [2009]; extrapolated to 390 yr assuming constant locking) and 2010 *M*8.8 Maule earthquake (red: *Vigny et al.* [2011]). Their coseismic data are multiplied by a factor 5 to compensate for a more than 4 times larger slip event (see section 4.2). The line colors in Figures 5a and 5b correspond to different locations shown as colored circles in Figures 5f, which depicts the continental margins lithology (black) and temperature (blue).

consistent with GPS data recorded before the 2010 *M*8.8 Maule earthquake by *Ruegg et al.* [2009]. Beyond reach of typically land-based GPS stations, we observe minor interseismic uplift of at most 1.2 m above the oceanic plate that subducted for 20 m.

[43] The spatial evolution of the coseismic period roughly mirrors the interseismic pattern, but for small shifts of the hinge points (Figure 5d). During the event we observe a translation from initial vertical motions above the hypocenter to a final maximum uplift of 9.8 m at 70 km from the trench. This spatial pattern of uplift surrounding a region of subsidence in between 115 and 225 km from the trench agrees well with GPS data obtained during the 2010 *M*8.8 Maule event [*Vigny et al.*, 2011]. The amplitude of the coseismic GPS data, however, had to be multiplied by a factor 5 to match the numerical event that slipped roughly four times more (explained in section 4.2).

[44] Postseismic creep is most significant within 50 km from the trench, although a minor postseismic delay of reversal to subsidence of 20–100 years is observed beyond 250 km (Figure 5e).

3.3. Stress and Strength at the Thrust

[45] The above analysis is limited to what is observed 6.4 km above the thrust and at the surface and lacks insights into the physics at the thrust interface. Figure 6 depicts a zoom of the spatiotemporal evolution of the second invariant of the deviatoric stress tensor (top), yield strength (middle), and strength excess (bottom). To evaluate the intrinsic contributions of temperature and pressure we analyze the reference model (models 2 in Figure 2) and afterward describe the minor differences for models with less and more predefined frictional stability regimes (models 1 and 3 in Figure 2, respectively).

[46] The reference model (Figure 6, middle column) shows a general increase in deviatoric stresses up to about 175 km from the trench (Figure 6b). There deviatoric stresses start to decrease distinctly. This behavior identifies the change from a domain regulated by brittle or plastic strengths to a domain where the viscous or ductile strength limits maximum stresses (i.e., the spontaneous brittle-ductile transition). Deviatoric second invariant stresses within the active seismogenic zone, approximately indicated by the observed blue rupture extent lines, reach values ranging from 10 to 35 MPa (around an average of ~18 MPa). This interseismic pattern is interrupted by events with a sudden stress drop that starts at about 130 to 150 km. Rupture propagation occurs as stresses are rapidly increased as the rupture approaches, dropping them during the rupture to ~3–4 MPa lower than their initial value (for more explanation, we refer to *van Dinther et al.* [2013]). However, within 60 and beyond 175 km from the trench events instead increase stresses with up to ~4 MPa. These are postseismically relaxed up to the next event by afterslip in a velocity-strengthening regime and viscoelastic stress relaxation, respectively. The region below the more resistive continental lithospheric mantle (between 145 and 175 km) shows elevated deviatoric stresses and a complex pattern of many local intermittent stress changes.

[47] The contemporary evolution of the yield stress shows a similar increase with distance to the trench as depth and pressures increase as well (Figure 6e). During events, the dynamic reduction of the friction coefficient with slip rate briefly reduces the strength by at most 10 MPa within 175 (or

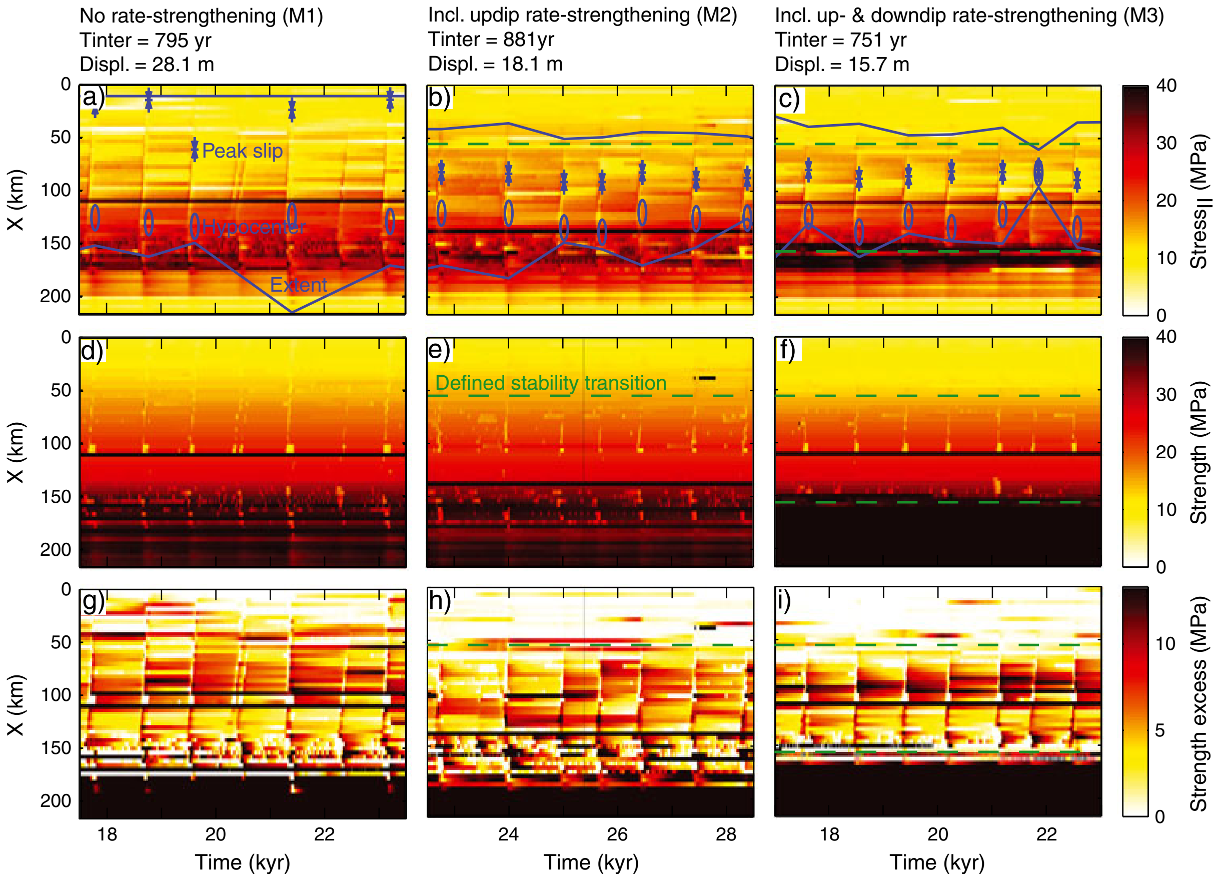

Figure 6. Spatiotemporal evolution at the thrust interface (defined by 55 equally spaced highest strain rate markers at t = 0) of (a–c) second invariant of the deviatoric stress tensor, (d–f) strength or yield stress, and (g–i) strength excess (i.e., rows 2 and 1) for three different models with no velocity strengthening (left column), the reference model with additional updip velocity strengthening (middle column), and additional downdip velocity strengthening (right column) (models 1, 2, and 3 in Figure 2). The dashed green lines indicate the predefined frictional stability limits. Blue symbols and lines in the top row mark the velocity-derived source parameters shown in black in Figure 4. X refers to the distance landward from the trench. *Tinter* and *Displ.* values provide average values for the entire 35,000 year series for recurrence interval and overriding plate displacement, respectively. Note that in all nonreference models the first 8,200 years are excluded to obtain a representative initial configuration. Note that the results described for models 1 and 3 are independent of an accompanying adjustment of the static friction coefficient as well.

occasionally 185) km from the trench. Within 65 km from the trench the strength is instead defined to increase. Local strength heterogeneities occur due to the occasional absence of highly overpressurized fluids (horizontal black lines in Figures 6d–6f).

[48] These observations are summarized in the strength excess (strength minus stress) that indicates how close a local point on the fault is to failure (Figure 6h). This reveals a heterogeneous and patchy spatiotemporal pattern. A negligible strength excess within ~50 km (T ~110°C) illustrates that the velocity-strengthening updip portion of the fault yields continuously and therefore creeps aseismically. The deeper portion of the fault (T >~450°C) shows a continuous very high strength excess in which the rupture is never able to penetrate as stresses are already viscously relaxed. For temperatures in between ~320°C and ~450°C we observe an erratic pattern with rapid strength excess decreases and increases indicative of very small events.

[49] If this occurs over a large enough patch a large unstable rupture nucleates. The nucleation of large events only occurs within the topmost part of this region where T <350°C (or between 4 and 14 km below the continental Moho). This hypocenter depth is observed to be mainly determined by the temperature-governed decrease in interseismic locking, rather than being below the continental Moho where stresses increase distinctly. Tests with a similar model and 1 My less subduction (and a hence warmer thrust fault zone) revealed a 17 km seaward shift of hypocenters. Additional tests show that the presence of the 1 km thin layer of serpentinites below the continental Moho (Figure 1b) reduces interseismic locking, thereby promoting a shallower downdip limit. All together, these tests document a large variability in rupture width, event size, and recurrence interval. This demonstrates the importance of geometry and rheology in determining earthquake source properties at subduction interfaces.

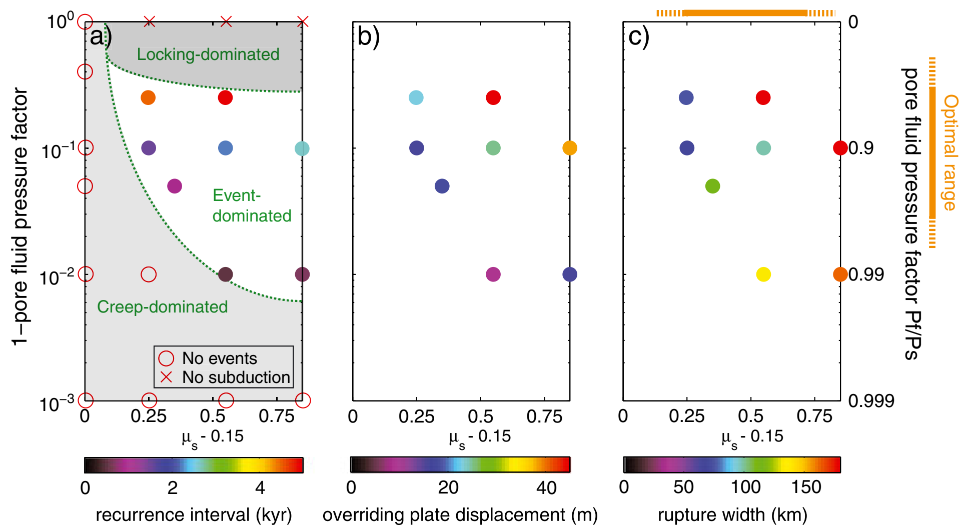

Figure 7. (a) Recurrence interval, (b) overriding plate displacement, and (c) rupture width averages for 21 models with different amounts of frictional weakening quantified as drop from static to a dynamic friction (X) versus different amounts of fluid-induced weakening in terms of $1 - P_f/P_s$ (Y). Green dotted lines in Figure 7a represent an estimate of the transitional borders between the three identified regimes. The orange range in Figure 7c indicates where results agree with observations. Models are run with a constant minimum dynamic friction coefficient of 0.15, which is near the average of the observed range for different rock types [*Di Toro et al.*, 2011]. Note that several models required significant time to obtain representative results.

[50] Defining the downdip or releasing the updip frictional stability conditions leads to the following minor differences with respect to these observations. Excluding velocity-strengthening friction for temperatures below 100°C–150°C (model 1 in Figure 2) leads to significantly wider and larger slip events that also recur slightly more often (Figure 6, left column). These events typically experience the fastest displacements at the trench, although heterogeneous low stresses and large strength excesses can force smaller ruptures to decelerate before reaching the trench. Shallow stresses are decreased as stress drops are larger, since slip is less constrained. Ruptures often break the trench even though interseismic aseismic creep occurs for most parts within 40 km from the trench due to low confining pressures.

[51] Adding velocity-strengthening friction for temperatures above 350°C–450°C (model 3 in Figure 2) replicates elastic modeling approaches and general patterns observed in laboratory experiments. This results in an increase of strength beyond 150 km (Figure 6, right column). Stress is correspondingly increased, even slightly updip of this transition, leading to slightly more (and smaller) events. Finally, we also observe that the occurrence of intermittent small events within the transition zone is significantly reduced.

3.4. Frictional Versus Fluid-Induced Weakening

[52] Figure 7 quantifies the amount of frictional and fluid-induced weakening necessary to sustain subduction and to generate unstable events. Fluid-induced weakening arises from an increase of pore fluid pressures P_f to values of $\lambda \cdot P_s$, if pore fluids are present. These pore fluids, resulting from compaction and slab dehydration, are present throughout most of the subduction channel (Figures 6d–6f). Frictional weakening occurs with increasing slip rate (equation (13)) and is represented in terms of a friction drop from static friction coefficient μ_s to the minimum dynamic friction coefficient μ_d.

[53] The 21 models in the strength diagram of Figure 7a can be subdivided into three regimes based on the seismogenic behavior of the interface. Viable models, which both show continuous regular subduction and a series of seismic events, are displayed as filled circles color coded by average recurrence interval. Crosses indicate models whose strength setup inhibits continuous conventional subduction as the original thrust interface is too strong. Models without fluid-induced weakening abandon the original thrust and initiate a new one cutting through the sedimentary wedge. If run at time steps common for geodynamic modeling (e.g., 100–1000 yr), these models show buckling of the continental margin. Open circles represent models whose strength combinations allow for subduction, but does not generate seismic events. This holds both for pore fluid pressures that are very near the lithostatic level (P_f/P_s = 0.999) and for models without frictional weakening ($\mu_s = \mu_d = 0.15$). These low-strength models show continuous creep along a very low viscosity thrust interface ($1 \cdot 10^{19}$ Pa s) with stresses on the order of 0–10 MPa.

[54] Within the viable strength domain in which events are observed (filled circles) the recurrence interval increases with increasing strength, both due to decreased pore fluid pressures and elevated static friction coefficients. Recurrence intervals increase from values near 530 years (for strengths of ~25 MPa at typical hypocenter depths of 30 km) up to ~7500 years (for strengths of ~120 MPa). The amount of coseismic displacement of the overriding plate increases in a similar manner with strength from 8 m to 68 m (Figure 7b). Rupture widths increase with strength as expected based on coseismic displacements (from 68 to

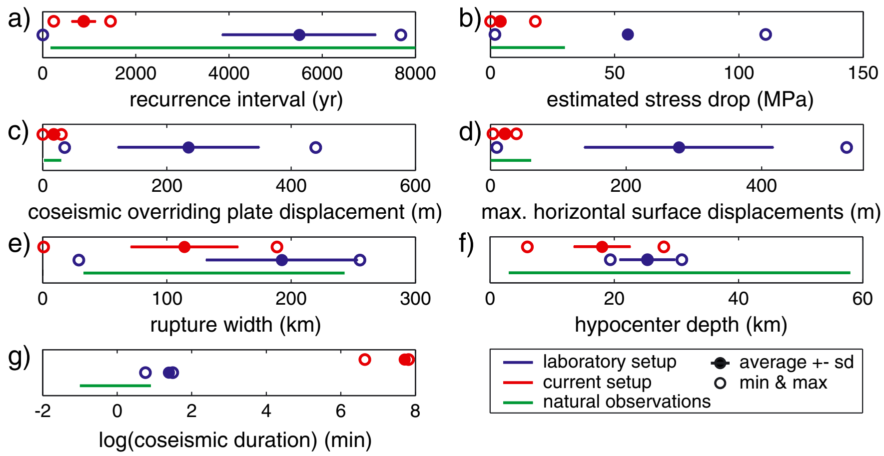

Figure 8. (a–g) Quantitative comparison of source and related parameters obtained in this study (red) with the numerical results obtained in the simplified laboratory setup (blue) [*van Dinther et al.*, 2013] and in relation to values observed in nature for normal to megathrust earthquakes (green line). Source parameter statistics are calculated (section 3.1) with hypocenter depth with respect to the trench (Figure 8f), while maximum horizontal surface displacement is calculated for all events at the central, magenta marker (Figure 5f). (d) Stress drop values (Figure 8b) are not systematically derived, but represent an estimation of the average, minimum, and maximum values based on a nonzoomed Figure 6 and in *van Dinther et al.* [2013, Figures 7 and 8]. The natural range for large earthquakes (M_w>7.5) is determined based on, e.g., *Heuret et al.* [2011], *Blaser et al.* [2010], *Ben-Zion* [2008], and observations of several megathrust earthquakes (1960 M9.5 Valdivia, 2004 M9.2 Sumatra, and 2011 M9.0 Tohoku). Note that the peak displacement and rupture speeds are not shown to enhance visibility. They relate to and show the same features and offset as shown in the coseismic duration.

182 km), but for the lowest fault strength viable model (λ = 0.99, μ_s = 0.7 explained in section 4.5) (Figure 7c).

4. Discussion

[55] The results shed light on the occurrence of interplate seismicity at subduction thrusts and lead to several interesting implications. Below, we first discuss how our viscoelastoplastic seismo-thermo-mechanical approach is validated by a comparison with (a) natural and laboratory observations in terms of recurrence and source parameters (section 4.1), (b) GPS-recorded surface displacements (section 4.2), and (c) seismological and field observations in terms of rupture characteristics (section 4.3). Subsequently, we discuss implications relating to the physical mechanisms governing seismogenic zone limits (section 4.4) and the strength of subduction thrust faults and the need for weakening mechanisms (section 4.5). Section 4.6 closes with a summary of the main limitations and future research directions. These sections are supported by a cartoon that summarizes the spatial relations between different types of model results.

4.1. Comparing Cycle Parameters to Laboratory Model and Natural Data

[56] The validity of the presented continuum viscoelastoplastic approach was demonstrated in a laboratory setup by extensively comparing numerical [*van Dinther et al.*, 2013] and laboratory results [*Corbi et al.*, 2013]. Figure 8 compares the results presented in the current paper to (a) the scaled numerical results obtained in the laboratory setup using the same code and the same source parameter selection procedure [*van Dinther et al.*, 2013] and (b) a range of values observed for earthquakes on the megathrust with M > 7.5.

[57] A significant improvement, compared to the laboratory study [*van Dinther et al.*, 2013], can be observed in Figure 8 (red versus blue data). The amount of overriding plate displacement and its related surface displacements are reduced to within reasonable values for megathrust earthquakes. This improvement also applies to the related stress drop and recurrence interval. The reduced slip cf. laboratory experiments mainly results from an approximately three times larger shear modulus of the composite fault zone and bulk forearc rocks. Such an increase in rigidity leads to a faster stress buildup for equal displacements (equation (8)), which reduces the recurrence interval to the next event. At the same time, an increase in rigidity allows for smaller amounts of deformation for a given stress, which leads to less accumulated displacements that can be recovered coseismically [e.g., *Abe*, 1975; *van Dinther et al.*, 2013]. Reduced overriding plate displacements are also facilitated by a large reduction (many orders of magnitude) of the shear modulus of the (analog) slab. In this case, the elastic, no longer viscous, slab stores part of the potential elastic energy that is released within the slab and not in the overriding forearc (as confirmed in Figures 3e–3f and 5c–5d). These factors also lead to smaller rupture widths, which scale with overriding plate displacements and slip (Figure 7) [e.g., *Blaser et al.*, 2010].

[58] However, in terms of coseismic temporal components, we observe less agreement with natural observations. The discrepancy in coseismic duration and speeds increases from a factor six in the laboratory model to about eight orders of magnitude for this setup. This results from the fact

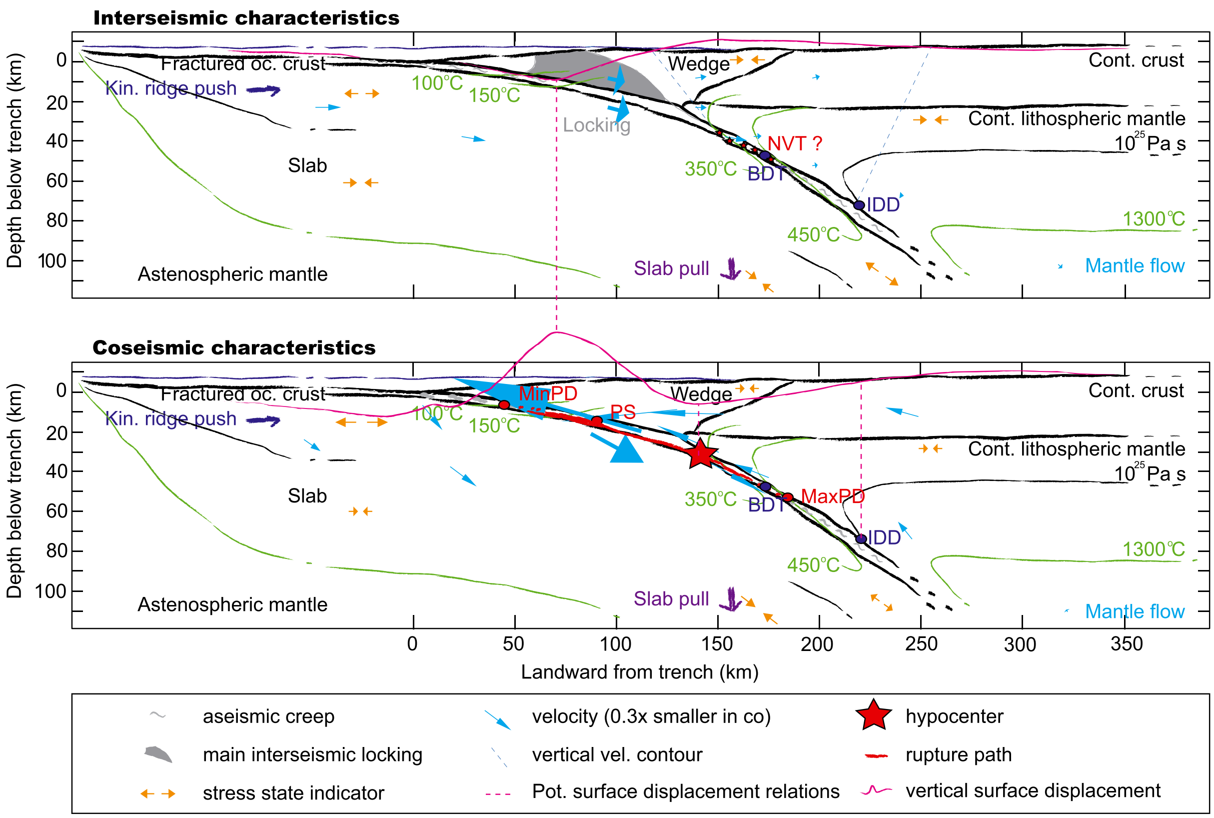

Figure 9. Schematic representation summarizing the (a) interseismic and (b) coseismic characteristics (based on Figures 1b, 3, 4a, 5c, 5d, 6b, 6e, and 6h). Contours of lithologies (black), sea level (purple), and isotherms (green) are included. Aseismic creep is defined by a viscosity lower than $1{\cdot}10^{20}$ Pa·s, while the main interseismic-locking patch is based on a minimum horizontal velocity of 3 cm/yr. BDT = brittle-ductile transition, IDD = interplate decoupling depth, NVT = nonvolcanic tremor, PS = peak coseismic displacement location, and PD = rupture penetration depth.

that we do not apply the dual temporal scaling [*Rosenau et al.*, 2009]. This was introduced in the laboratory setup to convert laboratory to natural values by assuming that inertia was more important than gravity during the coseismic period. The current large discrepancy suggests that further seismo-thermo-mechanical model improvements are required.

[59] Slow rupture propagation and stress release result from too low stress concentrations at the rupture front (and ahead of it). The (singular) stress concentration is smoothed as the blunt rupture tip is less well defined. This is also observed for anelastic fault zone models used in dynamic rupture modeling [*Dalguer and Day*, 2006]. In addition the fault zone width (up to hundreds of meters to a few thousand meters), in combination with a large time step (5 yr), decreases accelerations to an almost negligible level. This inhibits distinct shear wave propagation effects, while pressure waves are not simulated in any case. The absence of distinct seismic waves also reduces stress concentrations ahead of the rupture front further [e.g., *Ben-Zion and Rice*, 1997]. In a comparison between quasi-dynamic and fully dynamic models, the absence of inertial dynamics is also shown to reduce rupture and slip velocities [*Lapusta et al.*, 2000]. Furthermore, total slip is somewhat less as fault strength is not reduced by waves reflecting from the free surface. Overall, however, the qualitative behavior of the system is not expected to be largely affected by inertial dynamics [*Lapusta et al.*, 2000]. Since we are interested in the long-term seismic cycle pattern, for which slow tectonic loading and subsequent quasi-static nucleation are shown to be more important than the full inertial dynamics [*Lapusta et al.*, 2000, compare Figures 5, 14, and 15], we accept this severe limitation for now. This does mean that our single event dynamics is hampered. We do not distinguish foreshocks and aftershocks (and a potential early postseismic contribution), but rather depict the propagation of a single slow composite megathrust rupture. The occurrence of many consecutive events is rejected by the observation of a single nucleating and propagating rupture (Figures 3, 4, and 6) and the agreement with observed source parameters (Figures 5 and 6).

[60] The long-term seismic cycle response is quantified by recurrence interval and related parameters, such as stress drop, interface and surface displacements, and rupture width. These correspond well to megathrust earthquake observations (red versus green data in Figure 8), although displacements are on the large side of the spectrum of our limited spatiotemporal observation span. The correspondence to natural observations suggests that the dominant physical processes governing stress build up and

release, i.e., elasticity, frictional weakening, and gravity, are simulated properly.

4.2. GPS Displacements in Southern Chile

[61] Typically, models that evaluate static surface displacements use a relatively simple geometry in combination with a temporal pattern of either slip or stress change along a locked or partially locked fault [e.g., *Wang*, 2007]. The direct comparison to event data then requires tuning of several input parameters to reproduce the observed static displacements. Using our physically consistently evolving model, we captured the spatial pattern of the static GPS data recorded before and during the 2010 *M*8.8 Maule earthquake [*Ruegg et al.*, 2009; *Vigny et al.*, 2011] (Figures 5c–5d). This spatial agreement was only recognized after this figure was produced, so without tuning the model or event to the observations.

[62] This correspondence is facilitated by a similar spatial slip distribution (compare our Figure 4c with *Tong et al.* [2010], Figure 2b) and similar hypocenter location [*Moscoso et al.*, 2011]. The discrepancy in terms of a five times larger numerical coseismic vertical displacement magnitude is explained by the at least four times larger maximum differential slip at the numerical interface. The larger coseismic slip results from a 3.4 times longer strain accumulation period (595 instead of 175 years since the last "Darwin" earthquake) [*Darwin*, 1876] and an event-specific slip overshoot (as 1.33 times more displacement was recovered than was accumulated). This also explains why the interseismic data (both shown for a 390 yr interseismic period) do agree well without this slip correction. In summary, acknowledging the model was never tuned to match these surface data, this agreement demonstrates the applicability and strength of our physically consistent seismo-thermo-mechanical approach. We simulate interseismic locking and quasi-static rupture nucleation and propagation in a way comparable to nature. It further suggests that our physically evolved thermal, rheological, and structural models are well constrained. For the thermal part this is also supported by an agreement with thermal modeling results presented by *Gutscher* [2011].

[63] The general interseismic and coseismic surface displacements within the forearc (Figure 9) up to about 250 km agree with those observed and discussed in the laboratory setup [*van Dinther et al.*, 2013] and with the data and modeling results summarized in *Wang* [2007]. One interesting difference arises beyond 250 km from the trench, where we observe a second zone of interseismic subsidence and coseismic uplift (Figures 5c, 5d, and 9). This phenomenon is not present in the laboratory setup or in typical visco and/or elastic lithosphere modeling studies. This second coseismic hinge point is, however, observed for large megathrust earthquakes [e.g., *Plafker and Savage*, 1970; *Vigny et al.*, 2011; *Ikuta et al.*, 2012]. Three types of processes can potentially explain this phenomenon (Figure 9): (a) deep aseismic slip (60–85 km) [*Linde and Silver*, 1989], (b) elastic buckling due to compression of the overriding plate [*Vita Finzi and Mann*, 1994], and (c) a visco(elastic) response in the mantle wedge (a transient version of *Wdowinski et al.* [1989]). Quantitatively discriminating between these physical mechanisms is beyond the scope of this study.

[64] These physically consistent viscoelastoplastic models also recorded cycle-to-cycle variability of coseismic displacements and permanent deformation of the overriding plate (Figures 5a–5b). Cycle-to-cycle variability with positive and negative slip deficit of coseismic displacements with respect to the accumulated interseismic displacements is also tentatively observed for sections of the 2010 Maule earthquake [*Moreno et al.*, 2012; *Lin et al.*, 2013]. The observation that roughly 5% of overriding plate displacements is accommodated by permanent internal shortening agrees approximately with recent field observations [*Baker et al.*, 2013] and analog modeling results [*Rosenau et al.*, 2009].

4.3. Rupture Initiation, Propagation, and Complexity

[65] The described surface and source observables result from spontaneous nucleation and rupture propagation as explained in physical terms for the simplified laboratory setup [*van Dinther et al.*, 2013]. Most of the ruptures in the model initiate near the base of the seismogenic zone and propagate upward (95% in Figure 4a). This is also observed for abundant large earthquakes in nature [e.g., *Scholz*, 1988]. In our model hypocenters are typically located 4–14 km below the forearc Moho. This contradicts the idea that the forearc Moho acts as a structural limit [e.g., *Ruff and Tichelaar*, 1996]. It agrees with a compilation of global observations up to 2007, which confirmed that most seismogenic zones actually end well in the forearc mantle [*Heuret et al.*, 2011]. The locations of simulated hypocenters are mainly determined by temperature, which decreases viscosities (equation (9)) and locking thus introduces a stress gradient (Figures 3a, 3c, 3e, and 4a and section 4.4). The relation between such a strong viscosity drop and hypocenter locations has also been observed in other numerical models [*Huc et al.*, 1998]. Second, hypocenter locations are promoted by increased compression due to the strong overriding lithospheric mantle, which increases deviatoric stresses (Figures 3c and 6b).

[66] Subsequently, the rupture propagates through the composite fault zone selecting different paths in response to the current stress and strength distribution. This is amongst others influenced by previous ruptures and the stress history. Most ruptures propagate along one of the material interfaces (e.g., Figure 3b), as they experience largest differential slip rates. These preferred locations of shear localization agree with field observations on subduction channel melanges that were exhumed from depths just below the seismogenic zone [e.g., *Andersen and Austrheim*, 2006; *Bachmann et al.*, 2009; *Angiboust et al.*, 2012]. We also observe that the active fault zone typically widens as it approaches the surface (Figure 3b). The decrease in confining pressure and hence low-strength excess throughout the fault zone (Figure 6h) allows for more widespread faulting. This is more generally manner observed for strike-slip flower structures [e.g., *Woodcock and Fischer*, 1986] and in rupture models with off-fault damage [e.g., *Ma and Beroza*, 2008].

[67] The minor degree of complexity of the resulting seismic cycle pattern (Figure 4a) is introduced by heterogeneities in terms of (a) fault geometry (from cycle-to-cycle changing and undulating rupture paths; Figure 3b), (b) strength (e.g., fluid presence or not; Figure 6e), and (c) stress (Figure 6b). These heterogeneities are strong enough to deviate from a time-predictable sequence. Heterogeneities and

individual rupture patterns are, however, still simple enough to obtain a quasi-periodic and quasi-characteristic pattern. The observation of a quasi-periodic temporal recurrence for large (M >8) earthquakes agrees with various observations [e.g., *Kelleher et al.*, 1973] based on both paleoseismological studies [e.g., *Goldfinger et al.*, 2003] and numerical models [e.g., *Zöller et al.*, 2006]. However, considerable controversy about the complexity of subsequent rupture patterns still exists due to the limited observation period [e.g., *Rubinstein et al.*, 2012].

4.4. The Role of Temperature for the Downdip Seismogenic Zone Limit

[68] An understanding of the spatial extent of the seismogenic zone is important for hazard assessment, but physical mechanisms responsible for the updip and downdip limits remain without consensus [*Hyndman*, 2007]. We analyzed the self-consistent role of temperature, stress, and pressure dependence of viscosity that relates to the degree of interseismic locking (Figures 4, 5, and 6).

[69] For the downdip limit, without defining velocity-strengthening friction downdip (model 2 in Figure 2), we observe that events do not nucleate below 350°C, while they can not propagate beyond 450°C (Figures 6, 6b, 6e, 6h, and 9). The confinement to these limits results from the thermally (and stress) activated transition toward ductile shearing (i.e., spontaneous brittle-ductile, or rather plastic-ductile, transition BDT as seen in Figure 6b). The buildup of elastic stresses and successive rupture propagation is inhibited by rapid viscous relaxation as seen in numerical models from, e.g., *Huc et al.* [1998] and *Ellis and Stockhert* [2004]. The brittle-ductile transition has originally been thought to delineate the downdip limit of shallow earthquakes [e.g., *Sibson*, 1982]. However, in terms of a temperature-driven physical mechanism, it currently competes with velocity-strengthening friction, amongst other possible mechanisms. Velocity-strengthening friction also provides both frictional stability criteria for earthquake propagation and a mechanism for deep afterslip [e.g., *Tse and Rice*, 1986]. These two physical mechanisms are not similar but are likely to be closely related. Both their underlying deformation mechanisms relate to a change to a more ductile mechanism governing junction shear creep [e.g., *Shimamoto*, 1986; *Scholz*, 1988, 2002].

[70] The spontaneous downdip limit transition is also characterized by intermittent episodes of short stress drop and rapid stress increase (Figures 6b, 6e, and 6h). These small events are likely related to their location between two strong, moving, elastic lithosphere mantles (Figure 1b) and are facilitated by neighboring rapid stress changes. The shallow patches occasionally lead to the propagation of an instability, while the deeper, hotter ones can potentially be interpreted as failed nucleations, microseismicity, or as belonging to the families of slow slip [e.g., *Ide et al.*, 2007] or nonvolcanic tremor [e.g., *Obara*, 2002]. Including velocity-strengthening friction potentially inhibits these transition zone events. Since we want to influence unexpected feedback mechanisms as little as possible, we prefer not to define frictional stability constraints beyond those necessary to match first-order observations.

[71] The spontaneous occurrence of conditionally stable and stable-sliding regimes below a defined unstable section (Figures 6b and 9) agrees well with a range of observations [e.g., *Scholz*, 1988]. These domains are mainly determined by the temperature (and stress) feedbacks on viscosity and thereby on stress and elastic strain accumulation. The temperatures corresponding to these transitions (~350°C and ~450°C) also agree well with estimates from thermal modeling [e.g., *Oleskevich et al.*, 1999] and laboratory experiments on quartz and granite [e.g., *Blanpied et al.*, 1998]. These observations support the role of temperature in controlling the downdip limit of stable sliding and seismogenesis in this setup. However, we note that seismicity in several subduction zones warrants other mechanisms than those predicted by temperature, such as those related to pore fluid pressure and composition [e.g., *Hyndman et al.*, 1997; *Fagereng and Ellis*, 2009]. The accurate temperature agreement relates to the applied wet quartzite flow law (equation (9) and its laboratory-derived parameters in Table 1). This empirical law might inherently include the relevant transition of deformation mechanisms. The selection of a flow law describing more mafic rocks would have increased viscosities, locking, and the observed temperature limits.

4.5. Fault Strength: The Need for Both Frictional and Fluid-Induced Weakening

[72] The strength and related weakening of faults has long been intensely debated within several communities. High strengths (e.g., static friction coefficients of about 0.6–0.85) are supported by laboratory experiments [e.g., *Byerlee*, 1978], in situ stress measurements [e.g., *Brudy et al.*, 1997], and the orientation of faults [e.g., *Sibson and Xie*, 1998]. Other studies indicate that large (subduction) faults are actually weak (i.e., an effective friction coefficient below 0.10). The main arguments for this are based on an absent local heat flow anomaly [e.g., *Lachenbruch and Sass*, 1992], low angle geometrical considerations [e.g., *Suppe*, 2007], comparable margin parallel and perpendicular stresses [e.g., *Wang et al.*, 1995], and sustainable subduction in numerical models [e.g., *Zhong et al.*, 1998]. The three main candidates to weaken faults are (a) elevated fluid pressures [e.g., *Hubbert and Rubey*, 1959], (b) frictional weakening during earthquakes [e.g., *Di Toro et al.*, 2011], and (c) material with low static friction coefficients, such as talc [e.g., *Moore and Lockner*, 2008]. We broadly quantify the role of these mechanisms with respect to observations of both short-term earthquakes and long-term subduction characteristics.

[73] Varying the pore fluid pressure factor over a large range demonstrated that fluids, and weakening due to increased pore fluid pressures, are necessary to sustain regular subduction along the slab interface [e.g., *Gerya et al.*, 2008], even if frictional velocity weakening is present (locking-dominated domain in Figure 7a). However, fluid pressures cannot be equal to solid pressures (creeping-dominated domain in Figure 7a), as currently used in various long-term geodynamic models [e.g., *Mikhailov et al.*, 2013]. This leads to permanent creep at the thrust interface, which inhibits the buildup of elastic stresses necessary to generate earthquakes [*Faulkner and Rutter*, 2001].

[74] Within the event-dominated viable range, recurrence interval, slip, and rupture width increase with increasing strength (Figures 7a and 7b). Longer times are required to build up stresses to the strength limit. Once stresses

reach this higher strength limit, they can in fact drop further, leading to more slip over a wider area. This positive recurrence interval-slip relation was also observed in the laboratory setup [*van Dinther et al.*, 2013] and seems to quantitatively hold for natural observations as well [*Marzocchi et al.*, 2011]. However, the positive relation between slip and rupture width breaks down for the lowest fault strength model that still identified events ($\lambda = 0.99$, $\mu_s = 0.7$). This very low strength model has larger than expected rupture widths [e.g., *Mai and Beroza*, 2000], since the low stresses increase viscosities near the brittle-ductile transition (equation (9)). This extends interseismic locking downdip and leads to larger rupture widths.

[75] To obtain recurrence intervals and source parameters compatible with megathrust earthquakes, we infer that pore fluid pressure factors (P_f/P_s) are on average in the range of ~0.75 to ~0.99 (orange range in Figure 7c). We also infer that static friction coefficients could vary from at least 0.2–0.4 up to almost 1, if minimum dynamic friction is 0.15. This range of strength parameters is in agreement with certain worldwide pore fluid pressure factor estimates for subduction zones and Andean-type mountain building settings (0.80–0.98 in *Seno* [2009]) and various laboratory experiments ($0.5 < \mu_s < 1$ and $0.03 < \mu_d < 0.3$ for the range of lithologies analyzed at high speeds in *Di Toro et al.* [2011]). An additional very low static friction material, like talc, is not required to match the observables, although it could alternatively be invoked as long as bulk strengths are not too low to result in permanent creep. The corresponding low stress levels (below or near 20 MPa along most of the frictionally unstable thrust as in, e.g., Figure 3c) prevent detection of a heat flow anomaly and correspond to stress drop and orientation observations [*Hyndman*, 2007]. These inferences combined advocate that pore fluid pressures in subduction zones are indeed very high. This supports the claim that subduction thrust faults are (very) weak.

4.6. Model Limitations and Future Work

[76] The presented results generally demonstrate a satisfactory agreement with a wide range of long- and short-term natural observations, except for coseismic timescales (discussed as a major limitation in section 4.1). The temporal component also illustrated the spatial resolution limitation of a few hundreds of meters wide active fault interface (Figure 3). The overall thickness of the network of faults active over time, however, does fit observations of shear localizations within a subduction channel melange of hundreds to thousands of meters [e.g., *Shreve and Cloos*, 1986; *Fagereng and Sibson*, 2010] better than the typically used infinitely thin faults with an a priori, straight fixed geometry. Other important limitations are (a) the 2-D nature of the model, which ignores influential lateral effects and heterogeneities in interseismic stress build and coseismic rupture [e.g., *Kopp*, 2013], (b) a relatively simple friction model without a state component, and (c) the decoupled evolution of stresses and strengths if yielding is absent, i.e., throughout the interseismic period [*van Dinther et al.*, 2013]. To benefit from the feedback of self-consistent, long-term subduction dynamics [e.g., *Billen*, 2008; *van Dinther et al.*, 2010], we need to model a slab up to at least the 660 km discontinuity. Other future improvements include the analysis of off-megathrust rupture propagation (Y. van Dinther et al., Modeling the seismic cycle in subduction zones: The role and spatiotemporal occurrence of off-megathrust earthquakes, submitted to *Geophysical Research Letters*) and the implementation of fluid flow processes such that pore fluid pressure instead evolves as a function of permeability and stress [*Dymkova and Gerya*, 2013].

5. Conclusions

[77] This paper demonstrates the validity, strength, and limitations of a 2-D physically consistent, continuum viscoelastoplastic seismo-thermo-mechanical approach. This innovative approach simulates the feedback between long-term subduction dynamics and relating deformation and short-term seismogenesis. It also includes the three key ingredients for seismic cycle modeling in subduction zones: rate-dependent friction, slow tectonic loading, and viscoelastic stress relaxation. Its applicability is demonstrated by comparing results from a realistic setup of the Southern Chilean convergent margin (summarized in Figure 9) to a range of natural observations and competitive hypotheses.

[78] We observe a quasi-periodic pattern of quasi-characteristic *M*8–*M*9 interplate events every ~900 years (Figure 4). A quantitative natural comparison shows that all seismic cycle parameters are within the range observed for megathrust earthquakes, except for the coseismic temporal parameters (Figure 8). This suggests that elastic, frictional, and gravitational processes are captured well, while time stepping and inertial dynamics needs improvements.

[79] The spatial pattern of interseismic and coseismically recovering surface displacements agrees well with static GPS displacements observed before and during the 2010 *M*8.8 Maule earthquake (Figure 5). Without a single iteration to adapt either the numerical input data or the reference event, the displacements agree both qualitatively and, after a coseismic slip correction, also quantitatively. These interseismic and coseismic displacements highlight the presence of a second-order flexural bulge at distances of more than 200 km from the trench. On the long term, we observe that slip deficit varies from cycle-to-cycle and that about 5% of displacements are accommodated by permanent internal shortening.

[80] Qualitative coseismic features also agree with several seismological and geological observations. Ruptures typically nucleate 4–14 km below the forearc Moho and propagate upward along compositional boundaries, while widening as they approach the surface.

[81] The feedback from temperature (and stress) on viscosity introduces ductile shearing over a range that corresponds to the brittle-ductile transition (Figure 6). This (a) inhibits hypocenter locations at temperatures higher than ~350°C and (b) inhibits unstable rupture propagation beyond temperatures of ~450°C. These temperatures for the conditionally stable transition zone agree with results from thermal modeling and laboratory experiments, both obtained for the applied wet quartzite flow law. These observations confirm the dominant role of temperature in defining the downdip seismogenic zone limit in this specific setup.

[82] The main thrust fault is inferred to be very weak ($\sigma'_{\mathrm{II}} \approx$ 10–30 MPa) to sustain subduction and to generate typical recurrence intervals and slips of megathrust earthquakes (Figure 7). This mainly results from weakening due

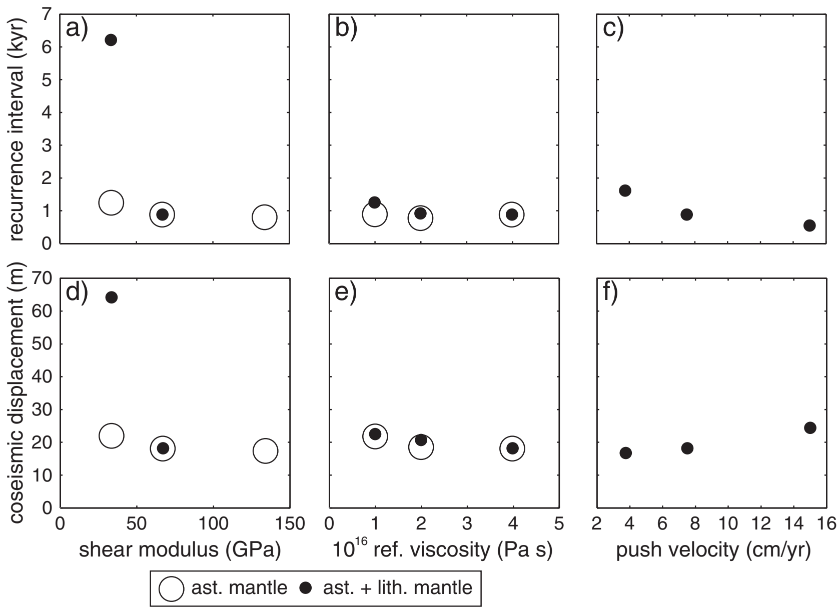

Figure B1. Effect of the (a, d) mantle's shear modulus, (b, e) mantle's reference viscosity η_0 (equation (9)), and (c, f) slab's push velocity on recurrence interval (Figures B1a–B1c) and coseismic overriding plate displacement (Figures B1d–B1f). Solid circles indicate a change in both lithosphere and asthenosphere mantle properties. Open circles indicate a change in asthenosphere mantle property only. For all nonreference models the first 8200 simulation years are excluded to obtain a more representative starting configuration. Note that this time span is not enough to obtain a new steady state equilibrium configuration with corresponding slab dip and related geometry, but it gives an indication of the impact of the parameters.

to increased pore fluid pressures (~0.75< λ <~0.99), which cannot be absent (i.e., λ = 0) as subduction along oceanic crust fails or lithostatic (i.e., λ = 0.999) as permanent creep results. Frictional weakening is required to introduce sufficient locking (and healing) to generate events (μ_s > 0.2–0.4 if μ_d = 0.15).

Appendix A: Laboratory-Based Derivation of Frictional Parameters

[83] The frictional properties of the subduction thrust interface are constrained by a few points taken from wet illite-rich gouge data obtained at seismogenic zone representative conditions up to temperatures of 500°C [*den Hartog et al.*, 2012]. As further explained below, we deviate from these laboratory measurements for (a) magnitude of characteristic velocity (to adapt to our low rupture speeds), (b) minimum dynamic friction coefficient [e.g., *Di Toro et al.*, 2011], and (c) temperature limits defining frictional stability regimes [e.g., *Blanpied et al.*, 1995].

[84] Frictional quantities for the three models are extracted at temperatures of 250°C, 300°C–375°C, and 450°C for the updip, central, and downdip regions. This provides values for the static friction coefficient μ_s and suggests relationships for the changes of characteristic velocity V_c and the amount of weakening γ between these three regions. To obtain reasonable characteristic velocities for our model, a viscoplastic characteristic slip velocity near the effectively transmitted subduction velocity is selected (V_c = 4.4 cm/yr = 1.4·10^{-9} m/s), as for the spring block derived data in *Corbi et al.* [2011] and *van Dinther et al.* [2013]. Subsequently, both updip and downdip characteristic velocities for velocity strengthening are set to about 1.5 times their velocity-weakening value (V_c = 6.3 cm/yr) [*den Hartog et al.*, 2012].

[85] To obtain minimum dynamic friction coefficients, we assume 70% of weakening. This amount is suggested to be characteristic for a wide range of rock types based on laboratory experiments at seismic slip speeds [*Di Toro et al.*, 2011] instead of experiments done at near-nucleation slip rate data [*den Hartog et al.*, 2012]. γ_{vw} = 0.7 corresponds to a minimum friction coefficients of 0.15 and an $a-b$ value of –0.0165 (using $V = 19.1 \cdot V_c$ in *Ampuero and Ben Zion* [2008, Appendix A]). Applying the relative sizes of *den Hartog et al.* [2012] the amount of updip strengthening should be ~2 times smaller (γ_{uvs} = –0.35 or $a-b$ = 0.0058). However, to compensate for a lack of lateral energy dissipation in our 2-D model and to prevent regular breaking of the trench [*van Dinther et al.*, 2013], we increase it by a factor two (γ_{uvs} = –1.5 or $a-b$ = 0.025). For model 3 the amount of strengthening in the downdip region is then 3 times higher than the strengthening updip (γ_{dvs} = –4.5 or $a-b$ = 0.12).

[86] We simplified the temperature profile to be consistent with often observed seismogenic zone limits [e.g., *Blanpied et al.*, 1995]. This avoids dependencies on laboratory ambiguities that are suggested to shift the $a-b$ neutral limits [*den Hartog and Spiers*, 2012]. The seismogenic zone limits are thus set to 100°C–150°C for the linear transition of updip velocity-strengthening to the velocity-weakening seismogenic zone and 350°C–450°C for the downdip linear

transition from velocity weakening to velocity strengthening [e.g., *Hyndman et al.*, 1997] (model 3 in Figure 2).

[87] Finally, note that we removed the downdip velocity-strengthening domain for the reference model (model 3 in Figure 2) to analyze the feedback from amongst others temperature on viscosity.

Appendix B: Subduction Velocity and Mantle Property Sensitivities

[88] To complement our analysis, we conduct a parameter study involving the applied push velocity and the viscoelastic properties of the mantle. The goal is to examine the sensitivity of the observed interplate seismicity and thereby obtain an indication for the importance of various model parameters. Subduction velocity turns out to be the geodynamic parameter with the highest correlation to interplate seismicity characteristics [*Heuret et al.*, 2011]. In terms of material parameters of the medium, the mantle viscosity has been found to be important, though only partially constrained [e.g., *Pollitz et al.*, 2000; *Forte and Mitrovica*, 2001]. Since most spontaneous rupture models do not consider the behavior of the Earth's mantle, we demonstrate its importance here.

[89] Recurrence interval and amount of coseismic displacement are observed to increase similarly with smaller mantle shear moduli (Figures B1a and B1d). This increase is particularly strong when the shear modulus of the interface-bounding lithospheric mantle is halved as well (solid circles). That leads to a more than six times larger recurrence interval and about three and a half times larger slip in events.

[90] Dividing asthenospheric mantle reference viscosity (η_0 in equation (9)) by a factor four (i.e., decreasing mantle viscosities by roughly two orders of magnitude) leads to an increase of at most a factor 1.4 of both recurrence interval and slip. The additional importance of decreasing the lithospheres reference viscosity as well is less prominent here, although it is still present for the recurrence interval.

[91] Applied slab push or subduction velocity plays a distinct role on interplate seismicity (Figures B1c and B1f). Decreasing subduction velocities increasingly increases recurrence intervals (+88% when halved with respect to the reference) and a contrasting, albeit smaller decrease of coseismic overriding plate displacement (–8% when halved).

[92] In summary, this brief sensitivity study shows variations of a factor 2 in kinematic and material parameters can impact interplate seismicity observables from as few as a factor 1.2 up to a factor of nearly 2 for subduction velocity and even up to a factor 6 for the lithosphere mantle's shear modulus.

[93] **Acknowledgments.** We thank Susan Ellis, an anonymous reviewer, and the Associate Editor for their constructive reviews. We warmly thank Francesca Funiciello and Fabio Corbi for stimulating discussions that improved the quality of this research. We also thank Christophe Vigny for providing the GPS data regarding the 2010 *M*8.8 Maule earthquake; Sabine den Hartog and Andre Niemeijer for providing their iolite friction data and related discussions; Arnauld Heuret for discussion on observational insights from subduction zone earthquakes; and Dave May, Thibault Duretz, Manuele Faccenda, and the KAUST HPC support for numerical assistance. This research was supported by SNSF grant 200021-125274 and the EURYI (European Young Investigators) Awards Scheme (Eurohorcs/ESF, responsible F.F.). Numerical models were run on the HPC clusters at ETH Zurich (Bigstar and Brutus) and KAUST (Neser).

References

Abe, K. (1975), Static and dynamic fault parameters of the Saitama earthquake of July 1, 1968, *Tectonophysics*, *27*(3), 223–238.

Ampuero, J.-P., and Y. Ben Zion (2008), Cracks, pulses and macroscopic asymmetry of dynamic rupture on a bimaterial interface with velocity weakening friction, *Geophys. J. Int.*, *173*, 674–692.

Andersen, T., and H. Austrheim (2006), Fossil earthquakes recorded by pseudotachylytes in mantle peridotite from the Alpine subduction complex of Corsica, *Earth Planet. Sci. Lett.*, *242*(1-2), 58–72.

Angiboust, S., P. Agard, P. Yamato, and H. Raimbourg (2012), Eclogite breccias in a subducted ophiolite: A record of intermediate-depth earthquakes?, *Geology*, *40*(8), 707–710.

Bachmann, R., O. Oncken, J. Glodny, W. Seifert, V. Georgieva, and M. Sudo (2009), Exposed plate interface in the European Alps reveals fabric styles and gradients related to an ancient seismogenic coupling zone, *J. Geophys. Res.*, *114*, B05402, doi:10.1029/2008JB005927.

Baker, A., R. W. Allmendinger, L. A. Owen, and J. A. Rech (2013), Permanent deformation caused by subduction earthquakes in northern Chile, *Nat. Geosci.*, *6*(6), 492–496.

Ben-Zion, Y. (2008), Collective behavior of earthquakes and faults: Continuum-discrete transitions, progressive evolutionary changes, and different dynamic regimes, *Rev. Geophys.*, *46*, RG4006, doi:10.1029/2008RG000260.

Ben-Zion, Y., and J. R. Rice (1997), Dynamic simulations of slip on a smooth fault in an elastic solid, *J. Geophys. Res.*, *102*, 17,771–17,784.

Billen, M. I. (2008), Modeling the dynamics of subducting slabs, *Annu. Rev. Earth Planet. Sci.*, *36*, 325–356, doi:10.1146/annurev.earth.36.031207.124129.

Bittner, D., and H. Schmeling (1995), Numerical modelling of melting processes and induced diapirism in the lower crust, *Geophys. J. Int.*, *123*(1), 59–70.

Blanpied, M. L., D. A. Lockner, and J. D. Byerlee (1995), Frictional slip of granite at hydrothermal conditions, *100*, 13,045–13,064.

Blanpied, M. L., C. J. Marone, D. A. Lockner, J. D. Byerlee, and D. P. King (1998), Quantitative measure of the variation in fault rheology due to fluid-rock interactions, *J. Geophys. Res.*, *103*, 9691–9712.

Blaser, L., F. Kruger, M. Ohrnberger, and F. Scherbaum (2010), Scaling relations of earthquake source parameter estimates with special focus on subduction environment, *Bull. Seismol. Soc. Am.*, *100*(6), 2914–2926.

Brackbill, J., and H. Ruppel (1986), FLIP: A method for adaptively zoned, particle-in-cell calculations of fluid flows in two dimensions, *J. Comput. Phys.*, *65*(2), 314–343.

Brudy, M., M. D. Zoback, K. Fuchs, F. Rummel, and J. Baumgärtner (1997), Estimation of the complete stress tensor to 8 km depth in the KTB scientific drill holes: Implications for crustal strength, *J. Geophys. Res.*, *102*, 18,453–18,475.

Buiter, S., A. Babeyko, S. Ellis, T. Gerya, B. Kaus, A. Kellner, G. Schreurs, and Y. Yamada (2006), The numerical sandbox: Comparison of model results for a shortening and an extension experiment, in *Analogue and Numerical Modelling of Crustal-Scale Processes,* vol. 253, edited by S. J. H. Buiter and G. Schreurs, pp. 29–64, Geological Society, London, Special Publication.

Burridge, R., and L. Knopoff (1967), Model and theoretical seismicity, *Bull. Seismol. Soc. Am.*, *57*(3), 341–371.

Byerlee, J. (1978), Friction of rocks, *Pure Appl. Geophys.*, *116*(4), 615–626.

Chester, F. M., and N. G. Higgs (1992), Multimechanism friction constitutive model for ultrafine quartz gouge at hypocentral conditions, *J. Geophys. Res.*, *97*(B2), 1859–1870.

Clauser, C., and E. Huenges (1995), Thermal conductivity of rocks and minerals, in *Rock Physics and Phase Relations: A Handbook of Physical Constants,* vol. 3, edited by T. J. Ahrens, pp. 105–126, American Geophysical Union Reference Shelf, AGU, Washington, D. C.

Cochard, A., and R. Madariaga (1994), Dynamic faulting under rate-dependent friction, *Pure Appl. Geophys.*, *142*(3/4), 419–445.

Connolly, J. A. D. (2005), Computation of phase equilibria by linear programming: A tool for geodynamic modeling and its application to subduction zone decarbonation, *Earth Planet. Sci. Lett.*, *236*(1-2), 524–541.

Corbi, F., F. Funiciello, C. Faccenna, G. Ranalli, and A. Heuret (2011), Seismic variability of subduction thrust faults: Insights from laboratory models, *J. Geophys. Res.*, *116*, B06304, doi:10.1029/2010JB007993.

Corbi, F., F. Funiciello, M. Moroni, Y. van Dinther, P. M. Mai, L. A. Dalguer, and C. Faccenna (2013), The seismic cycle at subduction thrusts: 1. Insights from laboratory models, *J. Geophys. Res. Solid Earth*, *118*, 1483–1501, doi:10.1029/2012JB009481.

Dalguer, L., and S. Day (2006), Comparison of fault representation methods in finite difference simulations of dynamic rupture, *Bull. Seismol. Soc. Am.*, *96*(5), 1764–1778.

Darwin, C. (1876), *Journal of Researches into the Natural History and Geology of the Countries Visited During the Voyage of the H.M.S. Beagle Round the World*, John Murray, London.

Del Gaudio, P., G. Di Toro, R. Han, T. Hirose, S. Nielsen, T. Shimamoto, and A. Cavallo (2009), Frictional melting of peridotite and seismic slip, *J. Geophys. Res.*, *114*, B06306, doi:10.1029/2008JB005990.

den Hartog, S. A. M., and C. J. Spiers (2012), Influence of subduction zone conditions and gouge composition on frictional slip stability of megathrust faults, *Tectonophysics*, *600*, 75–90.

den Hartog, S. A. M., A. R. Niemeijer, and C. J. Spiers (2012), New constraints on megathrust slip stability under subduction zone P–T conditions, *Earth Planet. Sci. Lett.*, *353-354*, 240–252.

Di Toro, G., R. Han, T. Hirose, N. D. Paola, S. Nielsen, K. Mizoguchi, F. Ferri, M. Cocco, and T. Shimamoto (2011), Fault lubrication during earthquakes, *Nature*, *471*(7339), 494–499.

Drucker, D., and W. Prager (1952), Soil mechanics and plastic analysis for limit design, *Q. Appl. Math.*, *10*, 157–165.

Dymkova, D., and T. Gerya (2013), Porous fluid flow enables oceanic subduction initiation on Earth, *Geophys. Res. Lett.*, *40*, doi:10.1002/2013GL057798.

Ellis, S., and B. Stockhert (2004), Elevated stresses and creep rates beneath the brittle-ductile transition caused by seismic faulting in the upper crust, *J. Geophys. Res.*, *109*, B05407, doi:10.1029/2003JB002744.

Escartin, J., G. Hirth, and B. Evans (1997), Nondilatant brittle deformation of serpentinites: Implications for Mohr-Coulomb theory and the strength of faults, *J. Geophys. Res.*, *102*(B2), 2897–2913.

Faccenda, M., L. Burlini, T. Gerya, and D. Mainprice (2008), Fault-induced seismic anisotropy by hydration in subducting oceanic plates, *Nature*, *455*(7216), 1097–1100.

Faccenda, M., T. V. Gerya, and L. Burlini (2009), Deep slab hydration induced by bending-related variations in tectonic pressure, *Nat. Geosci.*, *2*(11), 1–4.

Fagereng, A., and S. Ellis (2009), On factors controlling the depth of interseismic coupling on the Hikurangi subduction interface, New Zealand, *Earth Planet. Sci. Lett.*, *278*(1-2), 120–130.

Fagereng, A., and R. Sibson (2010), Mélange rheology and seismic style, *Geology*, *38*(8), 751–754.

Faulkner, D. R., and E. H. Rutter (2001), Can the maintenance of overpressured fluids in large strike-slip fault zones explain their apparent weakness?, *Geology*, *29*(6), 503–506.

Finzi, Y., E. H. Hearn, Y. Ben-Zion, and V. Lyakhovsky (2009), Structural properties and deformation patterns of evolving strike-slip faults: Numerical simulations incorporating damage rheology, *Pure Appl. Geophys.*, *166*, 1537–1573.

Forte, A., and J. Mitrovica (2001), Deep-mantle high-viscosity flow and thermochemical structure inferred from seismic and geodynamic data, *Nature*, *410*(6832), 1049–1056.

Furukawa, Y. (1993), Depth of the decoupling plate interface and thermal structure under arcs, *J. Geophys. Res.*, *98*(B11), 20,005–20,013, doi:10.1029/93JB02020.

Gerya, T. (2010a), Dynamical instability produces transform faults at mid-ocean ridges, *Science*, *329*, 1047–1050.

Gerya, T. (2010b), *Introduction to Numerical Geodynamic Modelling*, Cambridge Univ. Press, Cambridge, U. K.

Gerya, T., and D. A. Yuen (2007), Robust characteristics method for modelling multiphase visco-elasto-plastic thermo-mechanical problems, *Phys. Earth Planet. Inter.*, *163*(1-4), 83–105.

Gerya, T., J. Connolly, D. A. Yuen, W. Gorczyk, and A. M. Capel (2006), Seismic implications of mantle wedge plumes, *Phys. Earth Planet. Inter.*, *156*, 59–74.

Gerya, T. V., and F. I. Meilick (2011), Geodynamic regimes of subduction under an active margin: Effects of rheological weakening by fluids and melts, *J. Metamorph. Geol.*, *29*, 7–31.

Gerya, T. V., and D. A. Yuen (2003a), Characteristics-based marker-in-cell method with conservative finite-differences schemes for modeling geological flows with strongly variable transport properties, *Phys. Earth Planet. Inter.*, *140*(4), 293–318.

Gerya, T. V., and D. A. Yuen (2003b), Rayleigh–Taylor instabilities from hydration and melting propel 'cold plumes' at subduction zones, *Earth Planet. Sci. Lett.*, *212*(1), 47–62.

Gerya, T. V., J. A. Conolly, and D. A. Yuen (2008), Why is terrestrial subduction one-sided?, *Geology*, *36*(1), 43–46.

Goldfinger, C., C. H. Nelson, and J. E. Johnson (2003), Holocene earthquake records from the Cascadia subduction zone and Northern San Andreas fault based on precise dating of offshore turbidites, *Annu. Rev. Earth Planet. Sci.*, *31*(1), 555–577.

Gorczyk, W., A. Willner, T. Gerya, J. Connolly, and J. Burg (2007), Physical controls of magmatic productivity at Pacific-type convergent margins: Numerical modelling, *Phys. Earth Planet. Inter.*, *163*(1-4), 209–232.

Gutscher, M.-A. (2011), The Feb. 2010 M8.8 Maule Chile earthquake: Aftershock study from a temporary marine seismic network and thermal modeling of the subduction interface, *Pap. 35-11*, presented at 2011 GSA Fragile Earth Meeting, Munich, Germany, 4–7 Sep.

Heimpel, M. (2006), Earthquake scaling: The effect of a viscoelastic asthenosphere, *Geophys. J. Int.*, *166*(1), 170–178.

Heuret, A., and S. Lallemand (2005), Plate motions, slab dynamics and back-arc deformation, *Phys. Earth Planet. Inter.*, *149*, 31–51.

Heuret, A., S. Lallemand, F. Funiciello, C. Piromallo, and C. Faccenna (2011), Physical characteristics of subduction interface type seismogenic zones revisited, *Geochem. Geophys. Geosyst.*, *12*, Q01004, doi:10.1029/2010GC003230.

Hilairet, N., B. Reynard, Y. Wang, I. Daniel, and S. Merkel (2007), High-pressure creep of serpentine, interseismic deformation, and initiation of subduction, *Science*, *318*, 1910–1913.

Hirahara, K. (2002), Interplate earthquake fault slip during periodic earthquake cycles in a viscoelastic medium at a subduction zone, *Pure Appl. Geophys.*, *159*(10), 2201–2220.

Hofmeister, A. M. (1999), Mantle values of thermal conductivity and the geotherm from phonon lifetimes, *Science*, *283*(5408), 1699–1706.

Hubbert, M. K., and W. W. Rubey (1959), Role of fluid pressure in mechanics of overthrust faulting: 1. Mechanics of fluid-filled porous solids and its application to overthrust faulting, *Geol. Soc. Am. Bull.*, *70*(2), 115–166.

Huc, M., R. Hassani, and J. Chery (1998), Large earthquake nucleation associated with stress exchange between middle and upper crust, *Geophys. Res. Lett.*, *25*(4), 551–554.

Hyndman, R. (2007), The seismogenic zone of subduction thrust faults: What we know and don't know, in *The Seismogenic Zone of Subduction Thrust Faults*, edited by T. Dixon and J. Moore, pp. 15–41, Columbia Univ. Press, New York.

Hyndman, R., M. Yamano, and D. Oleskevich (1997), The seismogenic zone of subduction thrust faults, *Isl. Arc*, *6*(3), 244–260.

Ide, S., G. Beroza, D. Shelly, and T. Uchide (2007), A scaling law for slow earthquakes, *Nature*, *447*(7140), 76–79.

Ikuta, R., M. Satomura, A. Fujita, S. Shimada, and M. Ando (2012), A small persistent locked area associated with the 2011 M_w9.0 Tohoku-Oki earthquake, deduced from GPS data, *J. Geophys. Res.*, *117*, B11408, doi:10.1029/2012JB009335.

Kagan, Y. Y., and D. D. Jackson (2013), Tohoku earthquake: A surprise?, *Bull. Seismol. Soc. Am.*, *103*(2B), 1181–1194.

Kaneko, Y., J. Avouac, and N. Lapusta (2010), Towards inferring earthquake patterns from geodetic observations of interseismic coupling, *Nat. Geosci.*, *3*, 363–369.

Kelleher, J., L. Sykes, and J. Oliver (1973), Possible criteria for predicting earthquake locations and their application to major plate boundaries of the Pacific and the Caribbean, *J. Geophys. Res.*, *78*(14), 2547–2585.

Kopp, H. (2013), Invited review paper: The control of subduction zone structural complexity and geometry on margin segmentation and seismicity, *Tectonophysics*, *589*, 1–16.

Krawczyk, C. M., et al. (2006), Geophysical signatures and active tectonics at the south-central Chilean margin, in *The Andes: Active Subduction Orogeny. Frontiers in Earth Sciences*, edited by O. Oncken et al., pp. 171–192, Springer, Berlin, Heidelberg, New York.

Kuehn, N. M., S. Hainzl, and F. Scherbaum (2008), Non-Poissonian earthquake occurrence in coupled stress release models and its effect on seismic hazard, *Geophys. J. Int.*, *174*(2), 649–658.

Lachenbruch, A. H., and J. H. Sass (1992), Heat flow from Cajon Pass, fault strength, and tectonic implications, *J. Geophys. Res.*, *97*(B4), 4995–5015.

Lapusta, N., and S. Barbot (2012), Models of earthquakes and aseismic slip based on laboratory-derived rate-and-state friction laws, in *The Mechanics of Faulting: From Laboratory to Real Earthquakes*, edited by A. Bizzarri and H. S. Bhat, pp. 153–207, Research Signpost, Trivandrum, Kerala, India.

Lapusta, N., J. Rice, Y. Ben-Zion, and G. Zheng (2000), Elastodynamic analysis for slow tectonic loading with spontaneous rupture episodes on faults with rate- and state-dependent friction, *J. Geophys. Res.*, *105*(B10), 23,765–23,789.

Lavier, L. L., W. R. Buck, and A. N. B. Poliakov (2000), Factors controlling normal fault offset in an ideal brittle layer, *J. Geophys. Res.*, *105*(23), 431–423.

Lin, Y.-n. N., et al. (2013), Coseismic and postseismic slip associated with the 2010 Maule Earthquake, Chile: Characterizing the Arauco Peninsula barrier effect, *J. Geophys. Res. Solid Earth*, *118*, 3142–3159, doi:10.1002/jgrb.50207.

Linde, A. T., and P. G. Silver (1989), Elevation changes and the great 1960 Chilean earthquake: Support for aseismic slip, *Geophys. Res. Lett.*, *16*(11), 1305–1308.

Lohrmann, J., N. Kukowski, C. Krawczyk, O. Oncken, C. Sick, M. Sobiesiak, and A. Rietbro (2006), Subduction channel evolution in brittle fore-arc wedges—A combined study with scaled sandbox experiments, seismological and reflection seismic data and geological field evidence, in *The Andes: Active Subduction Orogeny*, edited by O. Oncken et al., pp. 237–262, Springer, Berlin, Heidelberg, New York.

Lyakhovsky, V., and Y. Ben-Zion (2008), Scaling relations of earthquakes and aseismic deformation in a damage rheology model, *Geophys. J. Int.*, *172*(2), 651–662.

Lyakhovsky, V., and Y. Ben-Zion (2009), Evolving geometrical and material properties of fault zones in a damage rheology model, *Geochem. Geophys. Geosyst.*, *10*, Q11011, doi:10.1029/2009GC002543.

Ma, S., and G. C. Beroza (2008), Rupture dynamics on a bimaterial interface for dipping faults, *Bull. Seismol. Soc. Am.*, *98*(4), 1642–1658.

Mai, P., and G. Beroza (2000), Source scaling properties from finite-fault-rupture models, *Bull. Seismol. Soc. Am.*, *90*(3), 604–615.

Marzocchi, W., L. Sandri, A. Heuret, F. Funiciello, and A. Heuret (2011), On the frequency-magnitude distribution of converging boundaries, Trans. AGU Fall Meet. Suppl., presented at 2011 AGU Fall Meeting, San Francisco, Calif.

Mikhailov, V., V. Lyakhovsky, I. Panet, Y. van Dinther, M. Diament, T. Gerya, O. deViron, and E. Timoshkina (2013), Numerical modelling of post-seismic rupture propagation after the Sumatra 26.12.2004 earthquake constrained by GRACE gravity data, *Geophys. J. Int.*, *195*, 640–650, doi:10.1093/gji/ggt145.

Moore, D. E., and D. A. Lockner (2008), Talc friction in the temperature range 25°–400 °C: Relevance for fault-zone weakening, *Tectonophysics*, *449*(1-4), 120–132.

Moreno, M., et al. (2012), Toward understanding tectonic control on the Mw 8.8 2010 Maule Chile earthquake, *Earth Planet. Sci. Lett.*, *321*, 152–165.

Moresi, L., F. Dufour, and H. Mühlhaus (2003), A Lagrangian integration point finite element method for large deformation modeling of viscoelastic geomaterials, *J. Comput. Phys.*, *184*(2), 476–497.

Moscoso, E., I. Grevemeyer, E. Contreras-Reyes, E. R. Flueh, Y. Dzierma, W. Rabbel, and M. Thorwart (2011), Revealing the deep structure and rupture plane of the 2010 Maule, Chile earthquake (Mw = 8.8) using wide angle seismic data, *Earth Planet. Sci. Lett.*, *307*(1-2), 147–155.

Needleman, A. (1988), Material rate dependence and mesh sensitivity in localization problems, *Comput. Methods Appl. Mech. Eng.*, *67*(1), 69–85.

Obara, K. (2002), Nonvolcanic deep tremor associated with subduction in southwest Japan, *Science*, *296*(5573), 1679–1681.

Oleskevich, D., R. D. Hyndman, and K. Wang (1999), The updip and downdip limits to great subduction earthquakes: Thermal and structural models of Cascadia, south Alaska, SW Japan, and Chile, *J. Geophys. Res.*, *104*(B7), 14,965–14,991.

Pacheco, J., and L. Sykes (1992), Seismic moment catalog of large shallow earthquakes, 1900 to 1989, *Bull. Seismol. Soc. Am.*, *82*(3), 1306–1349.

Peacock, S. M. (1993), Large-scale hydration of the lithosphere above subducting slabs, *Chem. Geol.*, *108*(1), 49–59.

Plafker, G., and J. C. Savage (1970), Mechanism of the Chilean Earthquakes of May 21 and 22, 1960, *Geol. Soc. Am. Bull.*, *81*(4), 1001–1030.

Poliakov, A. N. B., P. A. Cundall, Y. Y. Podladchikov, and V. A. Lyakhovsky (1993), An explicit inertial method for the simulation of viscoelastic flow: An evaluation of elastic effects on diapiric flow in two and three layer models, in *Flow and Creep in the Solar system: Observations, Modeling and Theory*, edited by D. B. Stone and S. K. Runcorn, pp. 175–195, Kluwer Academic Publishers, Holland.

Pollitz, F. F., G. Peltzer, and R. Bürgmann (2000), Mobility of continental mantle: Evidence from postseismic geodetic observations following the 1992 Landers earthquake, *J. Geophys. Res.*, *105*(B4), 8035–8054.

Ranalli, G. (1995), *Rheology of the Earth*, 2nd ed., Chapman and Hall, London.

Reid, H. (1910), On mass-movements in tectonic earthquakes, in *The California Earthquake of April 18, 1906: Report of the State Earthquake Investigation Commission*, pp. 192, Carnegie Institution of Washington, Washington, D. C.

Rosenau, M., and O. Oncken (2009), Fore-arc deformation controls frequency-size distribution of megathrust earthquakes in subduction zones, *J. Geophys. Res.*, *114*, B10311, doi:10.1029/2009JB006359.

Rosenau, M., J. Lohrmann, and O. Oncken (2009), Shocks in a box: An analogue model of subduction earthquake cycles with application to seismotectonic forearc evolution, *J. Geophys. Res.*, *114*, B01409, doi:10.1029/2008JB005665.

Rubinstein, J. L., W. L. Ellsworth, K. H. Chen, and N. Uchida (2012), Fixed recurrence and slip models better predict earthquake behavior than the time- and slip-predictable models: 1. Repeating earthquakes, *J. Geophys. Res.*, *117*, B02306, doi:10.1029/2011JB008724.

Ruegg, J. C., A. Rudloff, C. Vigny, R. Madariaga, J. B. De Chabalier, J. Campos, E. Kausel, S. Barrientos, and D. Dimitrov (2009), Interseismic strain accumulation measured by GPS in the seismic gap between Constitución and Concepción in Chile, *Phys. Earth Planet. Inter.*, *175*, 78–85.

Ruff, L. J., and B. W. Tichelaar (1996), What controls the seismogenic plate interface in subduction zones?, in *Subduction Top to Bottom, Geophys. Monogr. Ser.,* vol. 96, edited by E. Bebout et al., pp. 105–111, AGU, Washington, D. C., doi:10.1029/GM096p0105.

Saffer, D. M., and H. J. Tobin (2011), Hydrogeology and mechanics of subduction zone forearcs: Fluid flow and pore pressure, *Annu. Rev. Earth Planet. Sci.*, *39*(1), 157–186.

Schmeling, H., et al. (2008), A benchmark comparison of spontaneous subduction models—Towards a free surface, *Phys. Earth Planet. Inter.*, *171*(1-4), 198–223.

Scholz, C. (1988), The brittle-plastic transition and the depth of seismic faulting, *Geol. Rundsch.*, *77*, 319–328.

Scholz, C. H. (2002), *The Mechanics of Earthquakes and Faulting*, Cambridge Univ. Press, Cambridge, U. K.

Schultz, R. A. (1995), Limits on strength and deformation properties of jointed basaltic rock masses, *Rock Mech. Rock Eng.*, *28*(1), 1–15.

Seno, T. (2009), Determination of the pore fluid pressure ratio at seismogenic megathrusts in subduction zones: Implications for strength of asperities and Andean-type mountain building, *J. Geophys. Res.*, *114*, B05405, doi:10.1029/2008JB005889.

Shimamoto, T. (1986), Transition between frictional slip and ductile flow for halite shear zones at room temperature, *Science*, *231*(4739), 711–714.

Shreve, R., and M. Cloos (1986), Dynamics of sediment subduction, melange formation, and prism accretion, *J. Geophys. Res.*, *91*(B10), 10,229–10,245.

Sibson, R. H. (1982), Fault zone models, heat flow, and the depth distribution of earthquakes in the continental crust of the United States, *Bull. Seismol. Soc. Am.*, *72*(1), 151–163.

Sibson, R. H., and G. Xie (1998), Dip range for intracontinental reverse fault ruptures: Truth not stranger than friction?, *Bull. Seismol. Soc. Am.*, *88*(4), 1014–1022.

Stein, S., R. J. Geller, and M. Liu (2012), Why earthquake hazard maps often fail and what to do about it, *Tectonophysics*, *562-563*, 1–25.

Suppe, J. (2007), Absolute fault and crustal strength from wedge tapers, *Geology*, *35*(12), 1127–1130.

Tong, X., et al. (2010), The 2010 Maule, Chile earthquake: Downdip rupture limit revealed by space geodesy, *Geophys. Res. Lett.*, *37*, L24311, doi:10.1029/2010GL045805.

Tse, S., and J. R. Rice (1986), Crustal earthquake instability in relation to the depth variation of frictional slip properties, *J. Geophys. Res.*, *91*(B9), 9452–9472.

Tsutsumi, A., and T. Shimamoto (1997), High-velocity frictional properties of gabbro, *Geophys. Res. Lett.*, *24*(6), 699–702.

Turcotte, D. L., and G. Schubert (2002), *Geodynamics*, 2nd ed., Cambridge Univ. Press, Cambridge, U. K.

van Dinther, Y., G. Morra, F. Funiciello, and C. Faccenna (2010), Role of the overriding plate in the subduction process: Insights from numerical models, *Tectonophysics*, *484*, 74–86.

van Dinther, Y., T. V. Gerya, L. A. Dalguer, F. Corbi, F. Funiciello, and P. M. Mai (2013), The seismic cycle at subduction thrusts: 2. Dynamic implications of geodynamic simulations validated with laboratory models, *J. Geophys. Res. Solid Earth*, *118*, 1502–1525, doi:10.1029/2012JB009479.

Vigny, C., et al. (2011), The 2010 Mw 8.8 maule megathrust earthquake of Central Chile, monitored by GPS, *Science*, *332*(6036), 1417–1421.

Vita Finzi, C., and C. D. Mann (1994), Seismic folding in coastal south central Chile, *J. Geophys. Res.*, *99*(B6), 12,289–12,299.

Wang, K. (2007), Elastic and viscoelastic models of crustal deformation in subduction earthquake cycles, in *The Seismogenic Zone of Subduction Thrust Faults*, edited by T. Dixon and J. Moore, pp. 540–575, Columbia Univ. Press, New York.

Wang, K., T. Mulder, G. C. Rogers, and R. D. Hyndman (1995), Case for very low coupling stress on the cascadia subduction fault, *J. Geophys. Res.*, *100*(B7), 12,907–12,918.

Wdowinski, S., R. J. O'Connell, and P. England (1989), A continuum model of continental deformation above subduction zones: Application to the Andes and the Aegean, *J. Geophys. Res.*, *94*(B8), 10,331–10,346.

Woodcock, N. H., and M. Fischer (1986), Strike-slip duplexes, *J. Struct. Geol.*, *8*(7), 725–735.

Zhong, S., M. Gurnis, and L. Moresi (1998), Role of faults, nonlinear rheology, and viscosity structure in generating plates from instantaneous mantle flow models, *J. Geophys. Res.*, *103*(B7), 15,255–15,268.

Zöller, G., S. Hainzl, Y. Ben-Zion, and M. Holschneider (2006), Earthquake activity related to seismic cycles in a model for a heterogeneous strike-slip fault, *Tectonophysics*, *423*(1-4), 137–145.